Bioinspired Sulfo Oxygen Bridges Optimize Interfacial Water Structure for Enhanced Hydrogen Oxidation and Evolution Reactions

Chengdong Yang,[1,§] Yun Gao,[2,§] Zhengyu Xing[3], Xinxin Shu,[1] Zechao Zhuang[2], Yueqing Wang,[1] Yijuan Zheng,[3], Shuang Li,[3] Chong Cheng,[3,], Dingsheng Wang,[2,]* Jintao Zhang,[1,]**

[1] Key Laboratory for Colloid and Interface Chemistry, Ministry of Education School of Chemistry and Chemical Engineering, Shandong University, Jinan 250100, China

[2] Engineering Research Center of Advanced Rare Earth Materials, Department of Chemistry, Tsinghua University, Beijing 100084, China

[3] College of Polymer Science and Engineering, State Key Laboratory of Polymer Materials Engineering, Sichuan University, Chengdu 610065, China

*Correspondence to: Prof. Chong Cheng, chong.cheng@scu.edu.cn; Prof. Dingsheng Wang, wangdingsheng@mail.tsinghua.edu.cn; Prof. Jintao Zhang, jtzhang@sdu.edu.cn

[§] These authors contributed equally to this work.

Supplementary Figures

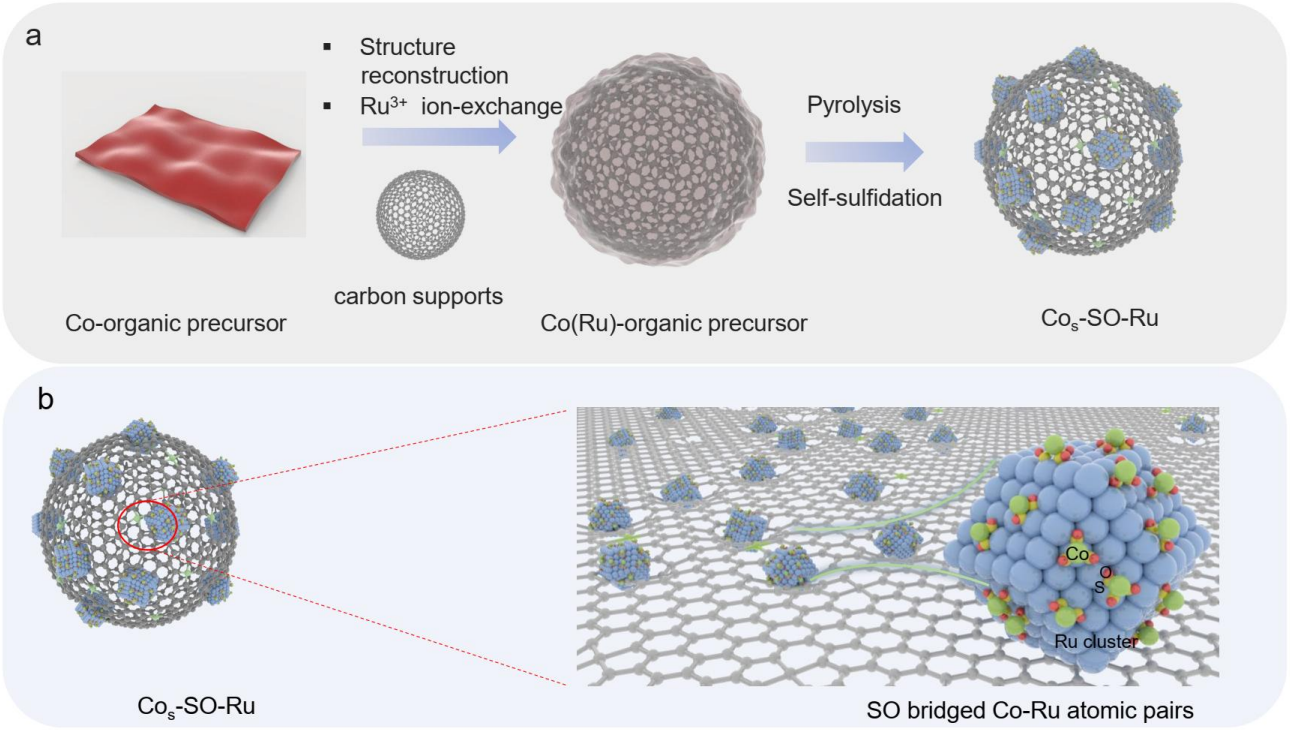

Supplementary Figure 1. a Schematic illustration of the synthetic processes of Co_s-SO-Ru. **b** Schematic illustration of the structure of Co_s-SO-Ru.

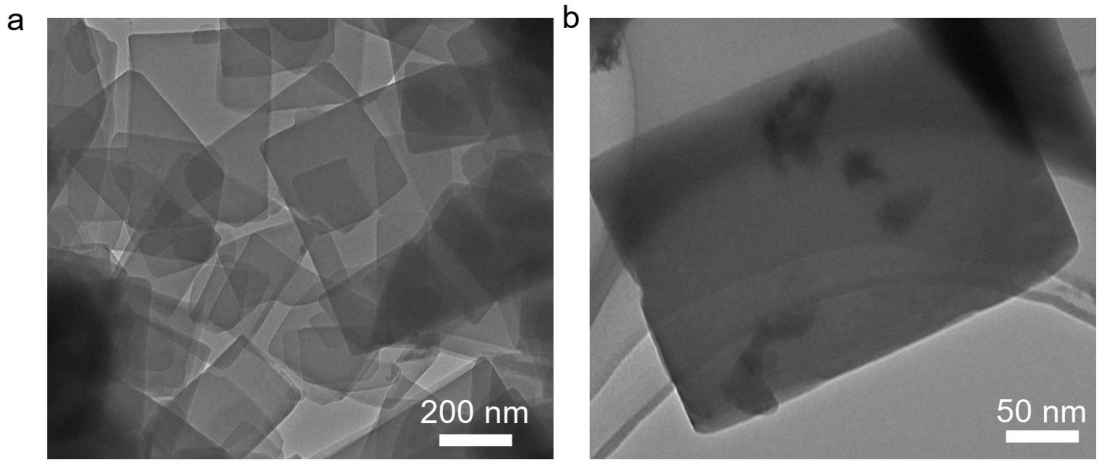

Supplementary Figure 2. a, b FE-SEM images of Co-organic precursor. As exhibited, the Co-organic precursor shows a typical 2D nanoplate that is consistent with previous reports.

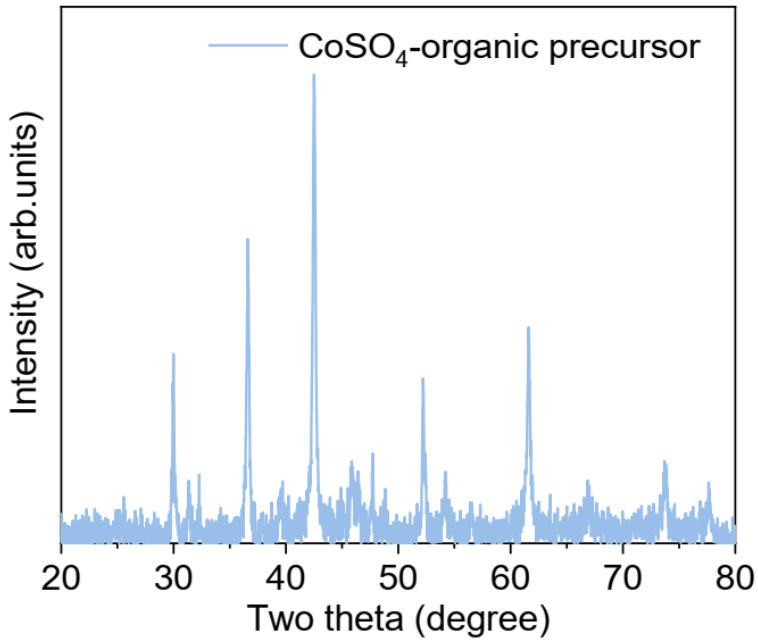

Supplementary Figure 3. XRD patterns of Co-organic precursor, which was prepared using $CoSO_4$ as Co source.

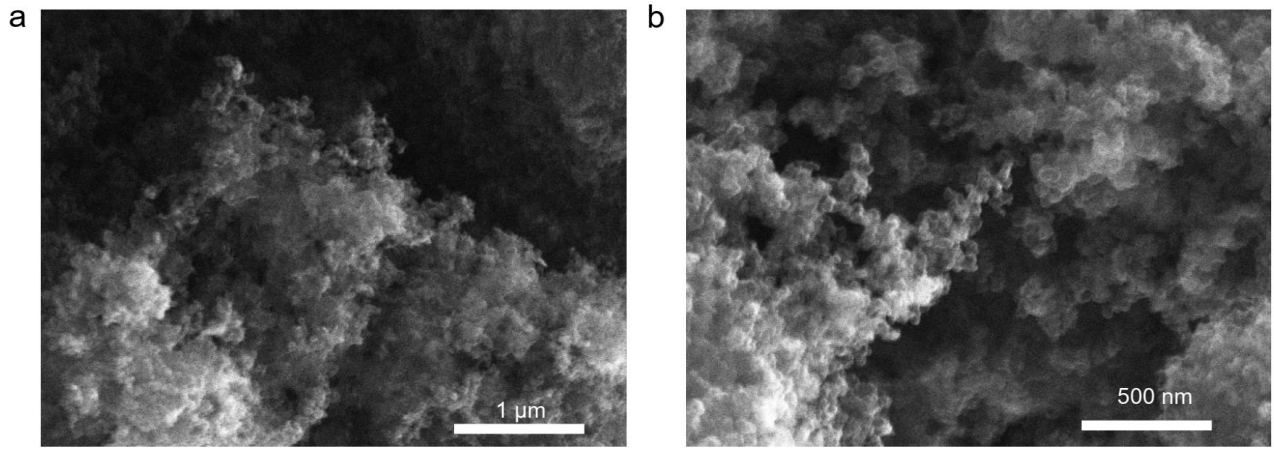

Supplementary Figure 4. a, b FE-SEM images of nanocarbon supported Co_s-SO-Ru.

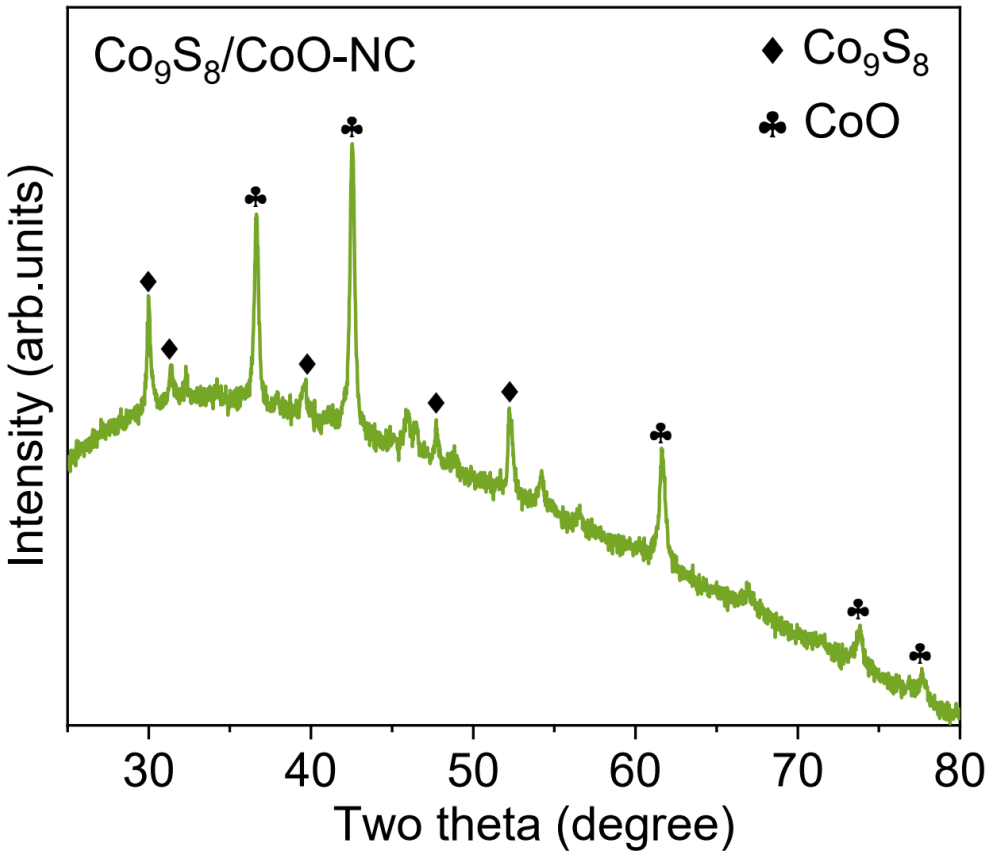

Supplementary Figure 5. XRD patterns of Co_9S_8/CoO-NC. The Co_9S_8/CoO-NC is obtained by pyrolyzing the Co-organic precursor under the Ar atmosphere without extra sulfur source. The formation of Co_9S_8 crystals can be attributed to the "self-sulfidation" procedure.

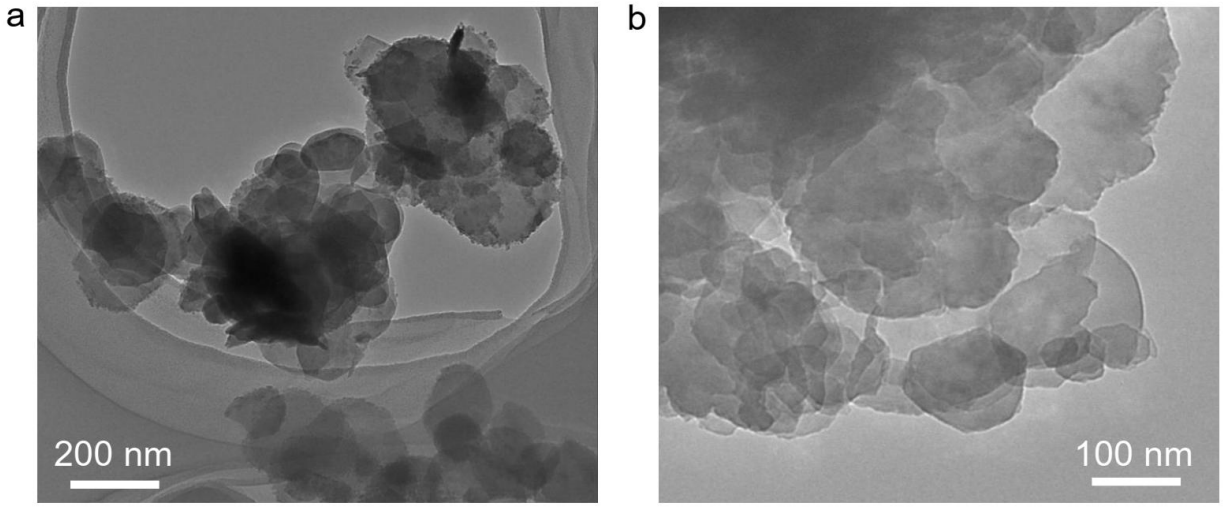

Supplementary Figure 6. a, **b** FE-SEM images of $CoNO_3$-organic precursor. The $CoNO_3$-organic precursor was synthesized based on the same process as the Co-organic precursor, except that the cobalt salt was changed to $Co(NO_3)_2$.

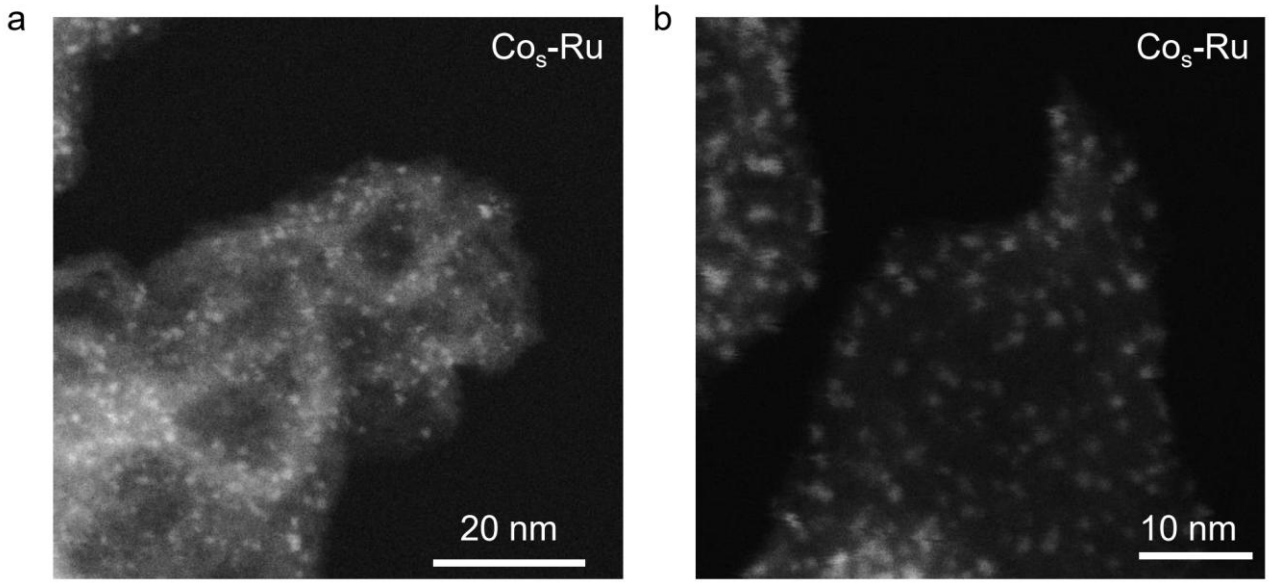

Supplementary Figure 7. a, **b** STEM images of the nanocarbon-supported Co_s-Ru.

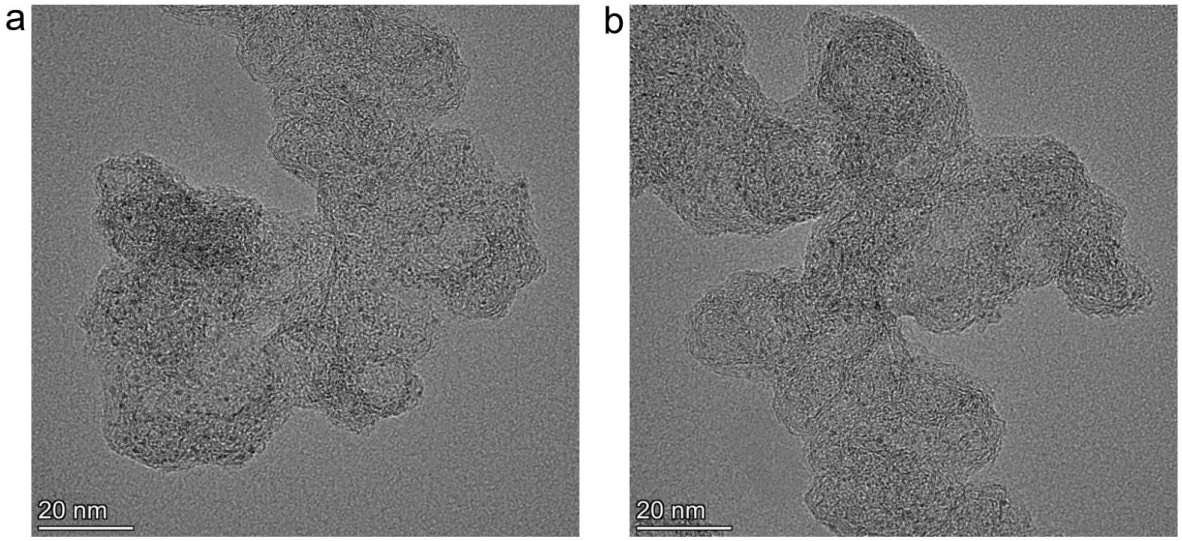

Supplementary Figure 8. a, **b** TEM images of the nanocarbon-supported Co_s-SO-Ru.

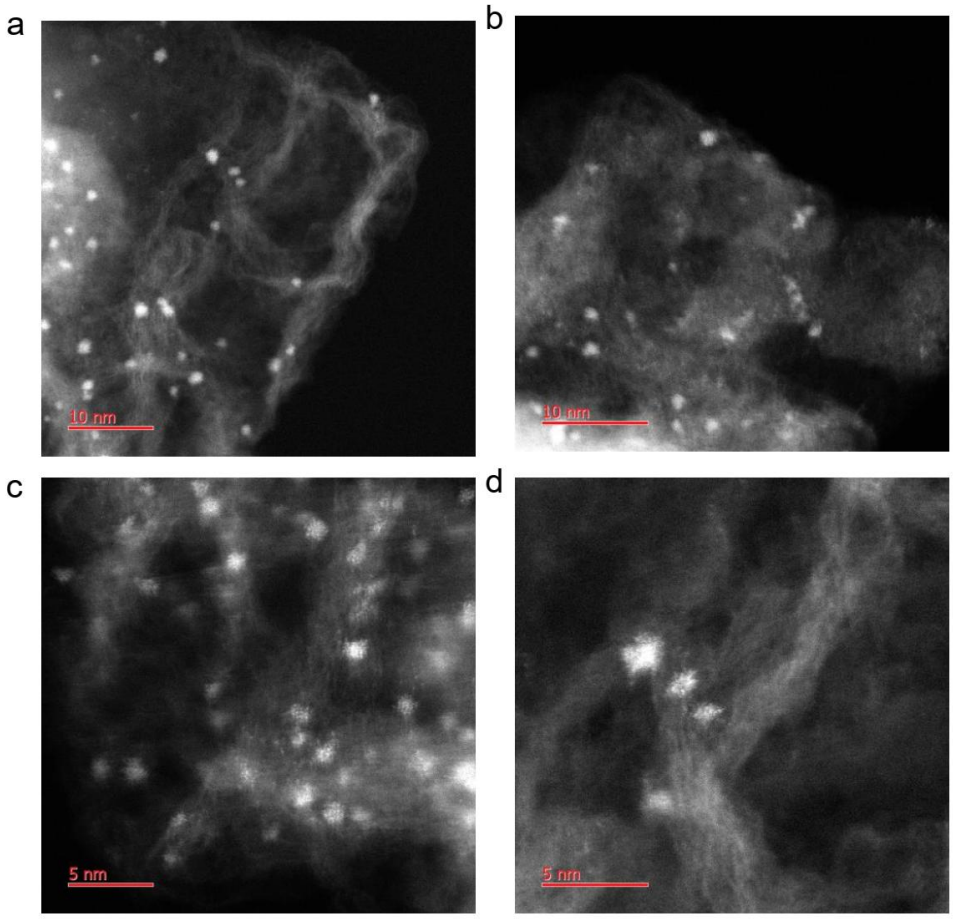

Supplementary Figure 9. a-d Atomic-resolution HAADF-STEM images of Co_s-SO-Ru.

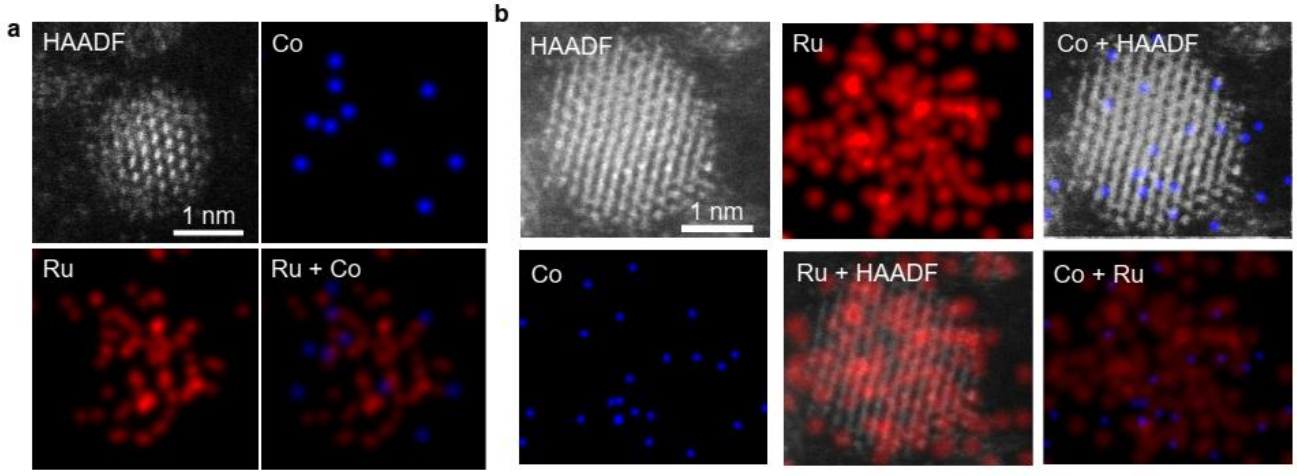

Supplementary Figure 10. a, **b** HAADF-STEM images of Co_s-SO-Ru and corresponding EDX mappings.

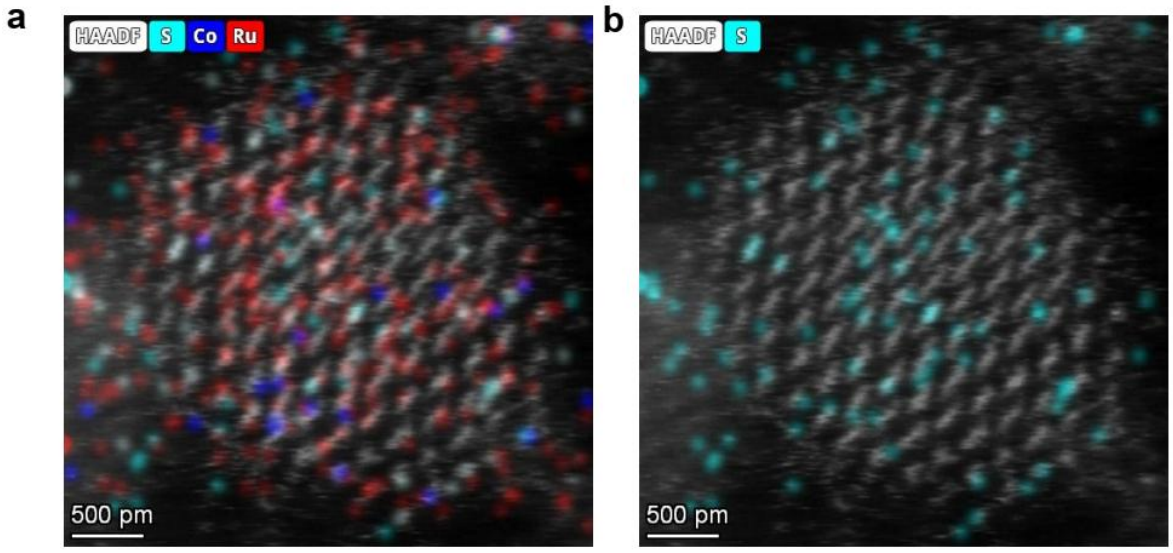

Supplementary Figure 11. a, **b** HAADF-STEM image of Co_s-SO-Ru and corresponding EDX mappings.

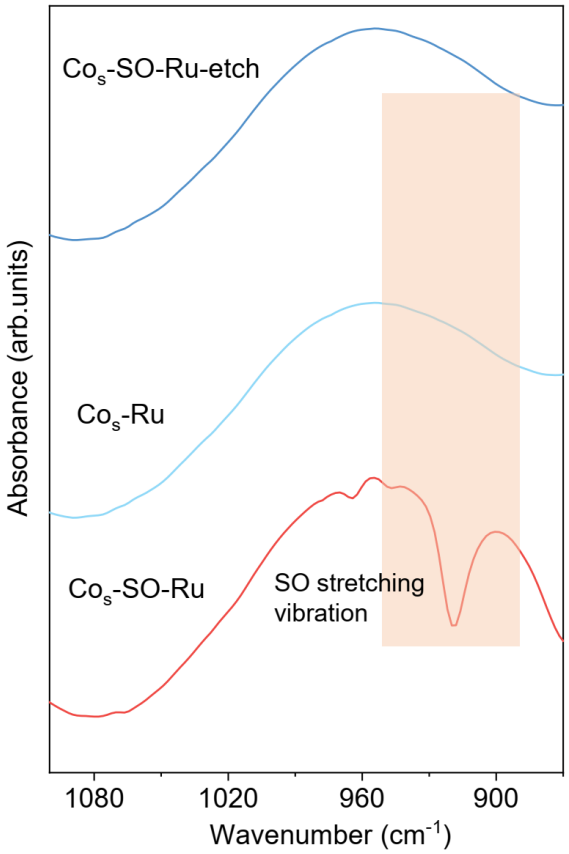

Supplementary Figure 12. FT-IR spectra of Co_s-SO-Ru, Co_s-Ru, and Co_s-SO-Ru-etch.

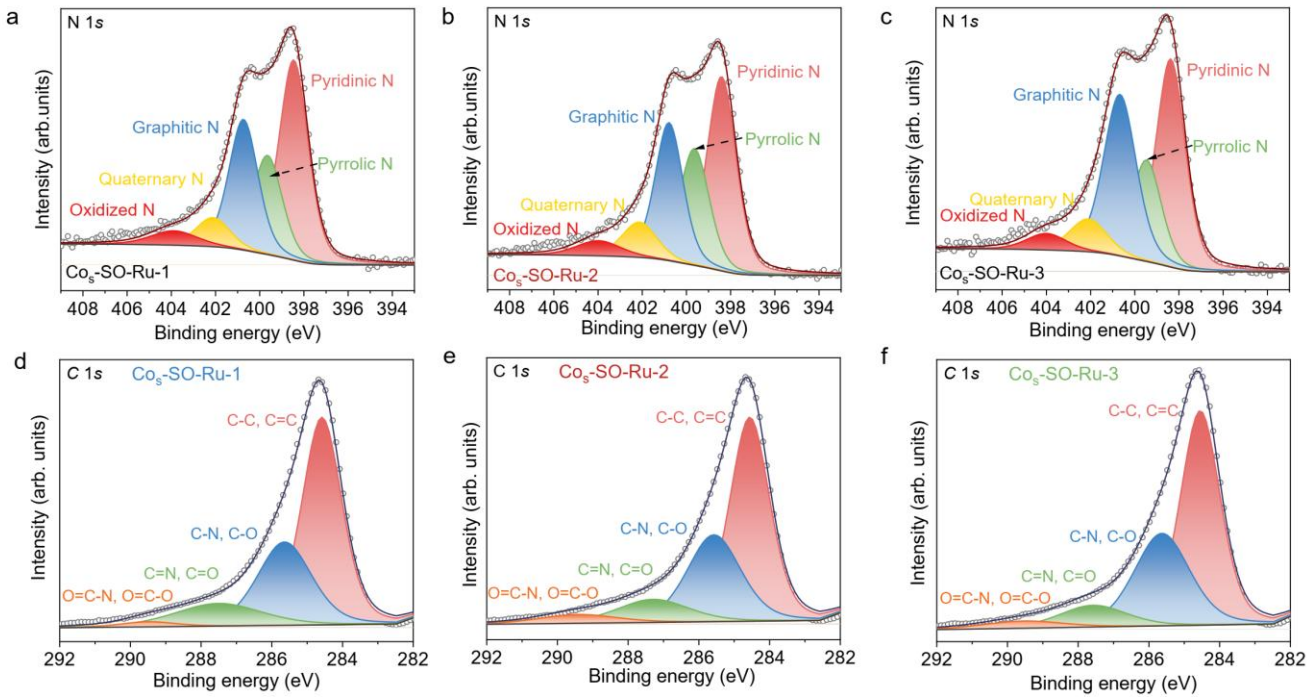

Supplementary Figure 13. a-c The N 1*s* XPS spectra of Co_s-SO-Ru-1/2/3. **d-f** The C 1*s* XPS spectra of Co_s-SO-Ru-1/2/3.

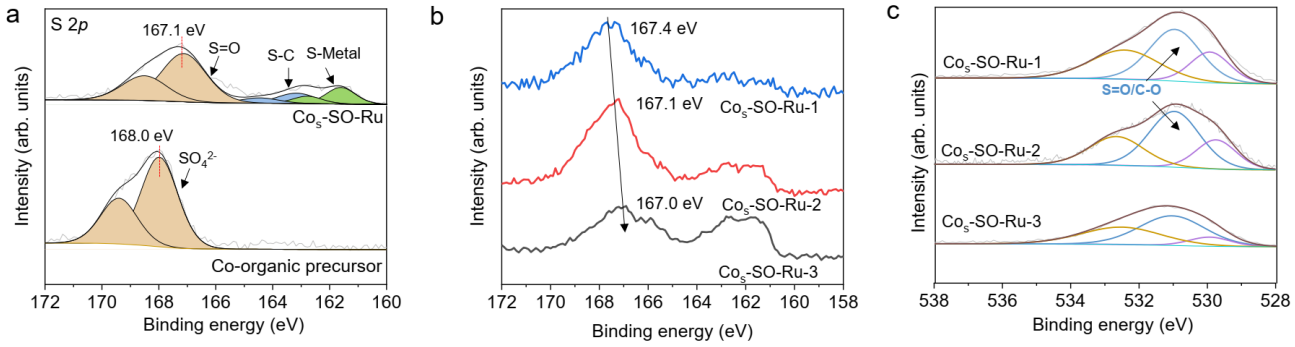

Supplementary Figure 14. a The S 2*p* XPS spectra of Co-organic precursor and Co$_s$-SO-Ru. **b** The S 2*p* XPS spectra of Co$_s$-SO-Ru-1/2/3. **c** The O 1*s* XPS spectra of Co$_s$-SO-Ru-500/600/700. The Co$_s$-SO-Ru-1/2/3 samples are obtained by pyrolyzing the Co(Ru)-organic precursor at 500, 600, and 700 ^{o}C, respectively. As shown, increasing the carbonization temperature results in a shift of the binding energy of S=O bonds to a lower position, indicating the deoxygenation process of SO_4^{2-} counter anion. Meanwhile, the decreased intensity of S=O peaks also demonstrate the reduction of SO_4^{2-} anion, which is likely facilitated by the reductive nature of the carbon support during pyrolysis. The increase in S-metal bond intensity further suggests that the S=O bonds are ultimately converted into metallic sulfide. Besides, with increasing the carbonization temperature, the decreased intensity of O 1*s* peaks would be attributed to the reduction of S=O bonds under higher carbonization temperatures.

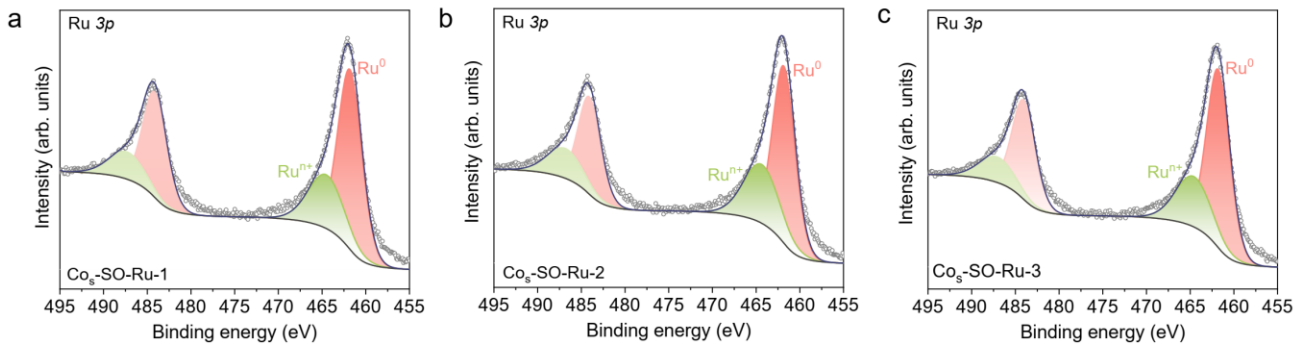

Supplementary Figure 15. a-c XPS spectra of Co_s-SO-Ru-1/2/3 in Ru 3*p* regions, which are obtained by introducing different contents of Ru species in Co_s-SO-Ru.

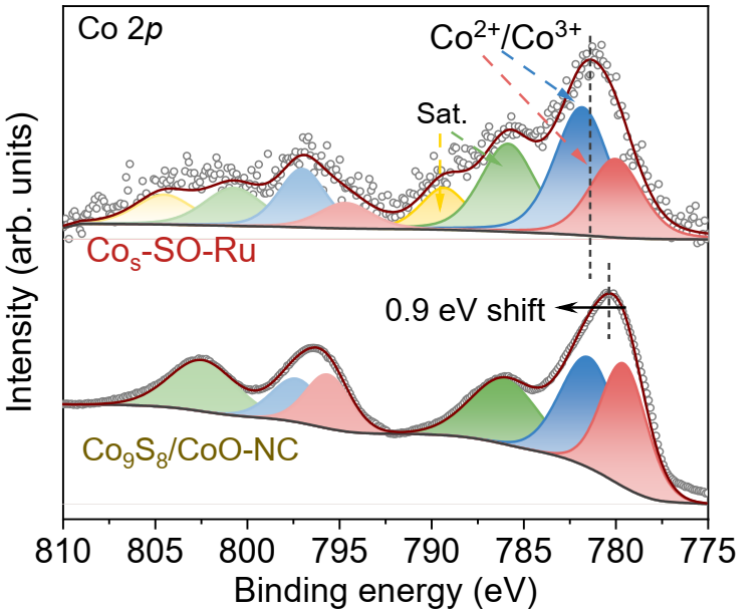

Supplementary Figure 16. The Co 2*p* XPS spectra of Co_s-SO-Ru and Co_8S_9/CoO-NC.

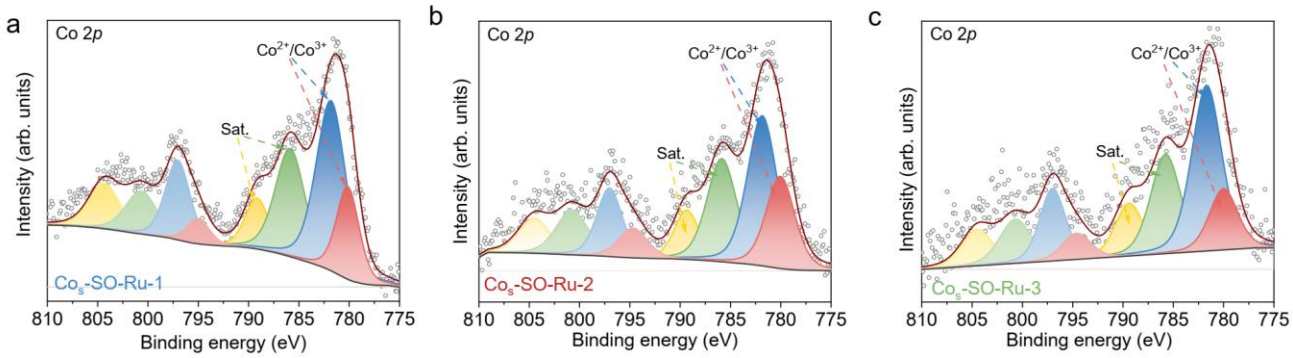

Supplementary Figure 17. a-c The Co 2*p* XPS spectra of Co_s-SO-Ru-1/2/3.

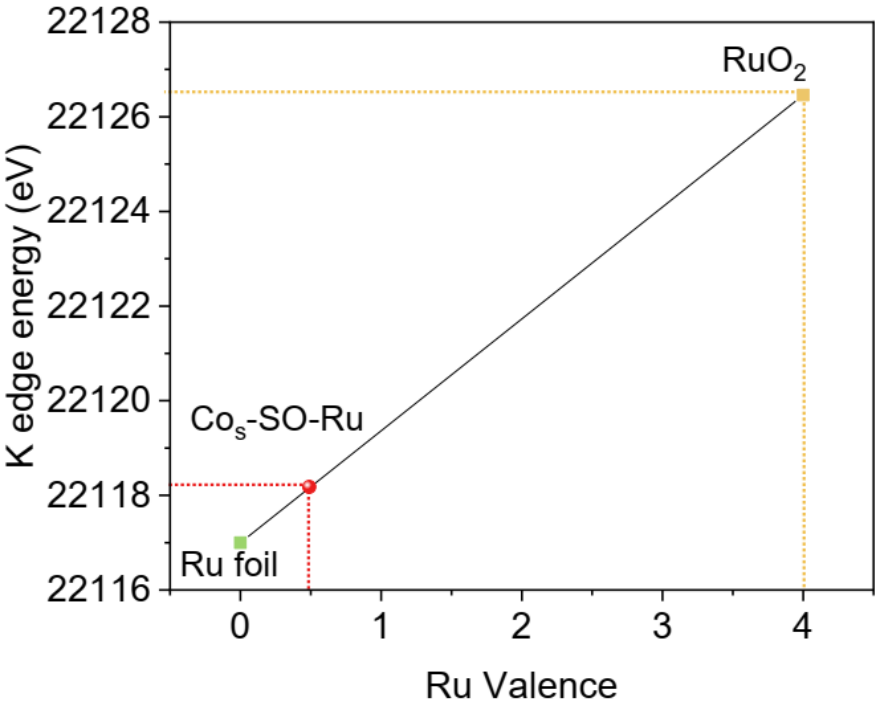

Supplementary Figure 18. The valence analysis of Ru elements in Ru foil, Co_s-SO-Ru, and RuO_2.

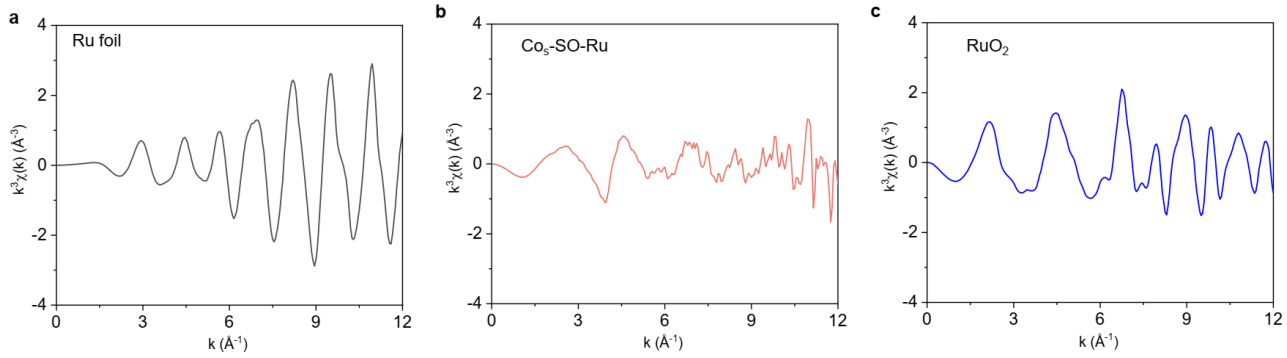

Supplementary Figure 19. The k^3-weighted EXAFS curves of Ru *K*-edge in *k*-space for **a** Ru foil, **b** Co_s-SO-Ru, and **c** RuO_2.

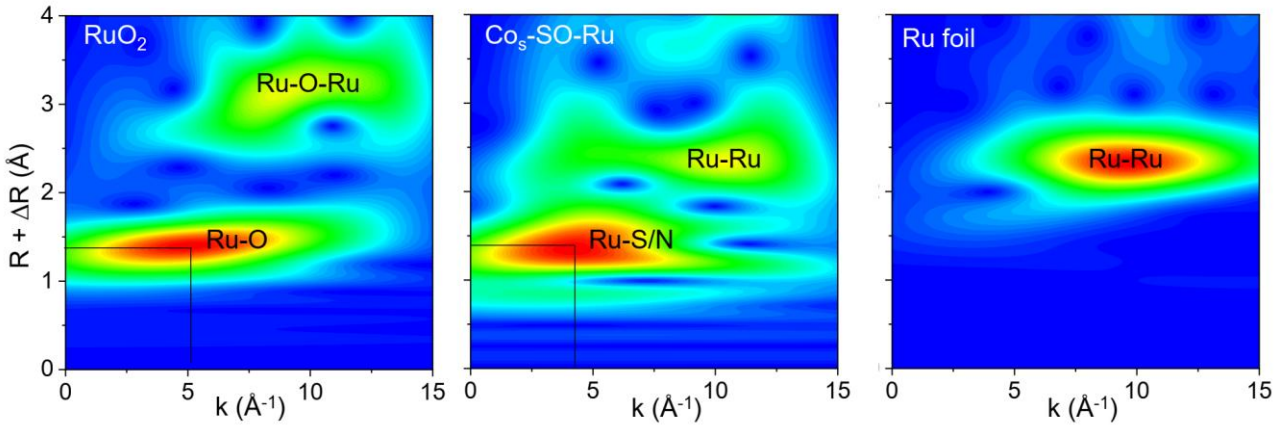

Supplementary Figure 20. WT-EXAFS for Ru foil, Co_s-SO-Ru, and RuO_2. WT-EXAFS images for Co_s-SO-Ru exhibit slightly longer Ru-S/N bonds than Ru-O bonds, indicating the mixture coordination of Ru-S/N with the relatively long Ru-S bonds.

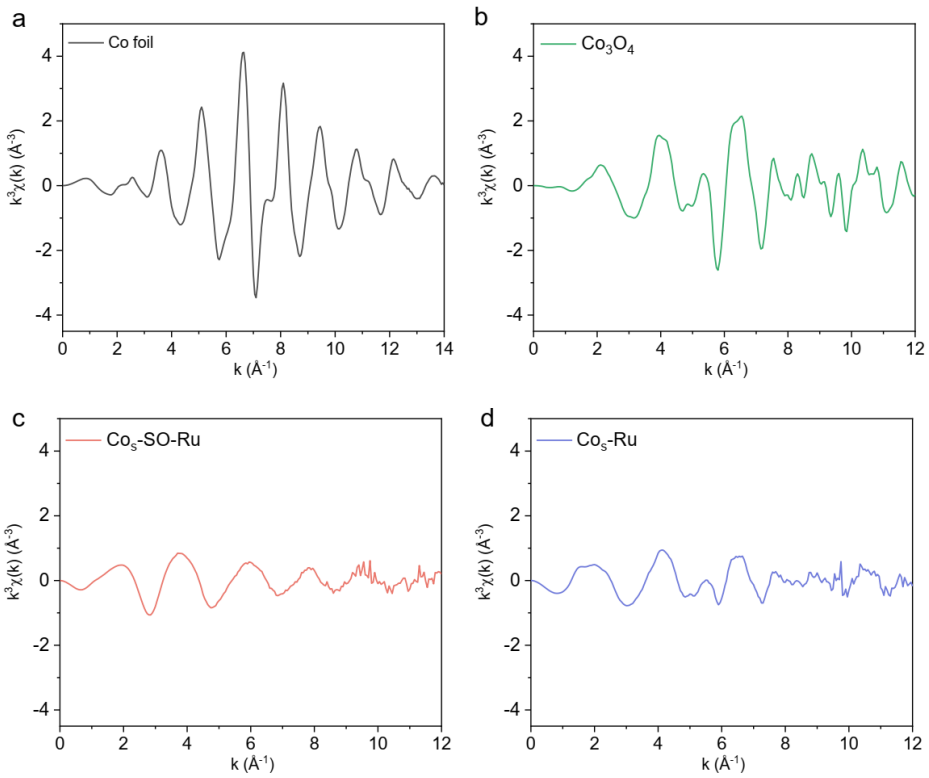

Supplementary Figure 21. The k^3-weighted FT curves of Co *K*-edge in *k*-space for **a** Co foil, **b** Co_3O_4, **c** Co_s-SO-Ru, and **d** Co_s-Ru.

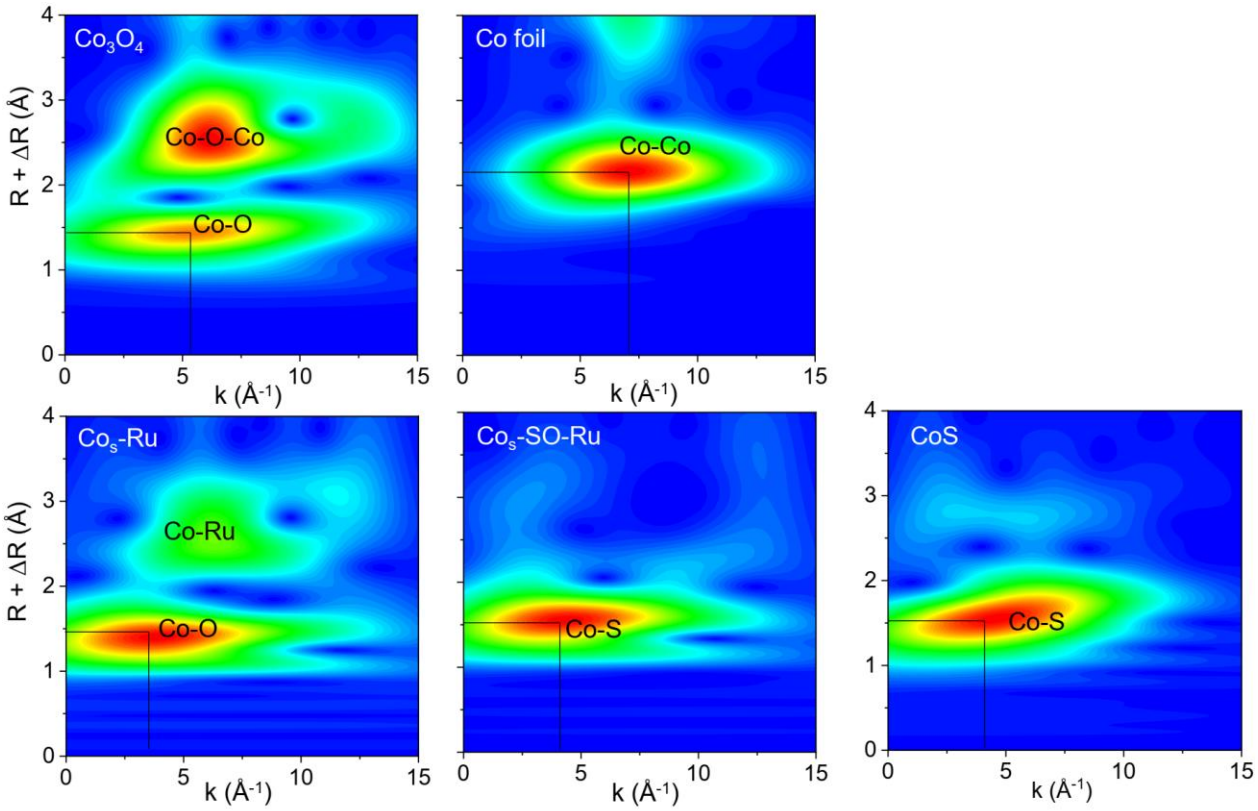

Supplementary Figure 22. WT-EXAFS for Co foil, Co_3O_4, Co_s-Ru, and Co_s-SO-Ru. Importantly, WT images at the Co *K*-edge show the predominant Co-S bonds (2.23 Å) in the first coordination shell similar with that of CoS, demonstrating the formation of sulfo-oxygen bonds bridged Co single-atoms. Besides, the Co_s-Ru exhibits a longer Co-Ru bond than that of Co-Co bond in Co foil, confirming that the Co single-atoms are doped onto the surface of Ru clusters.

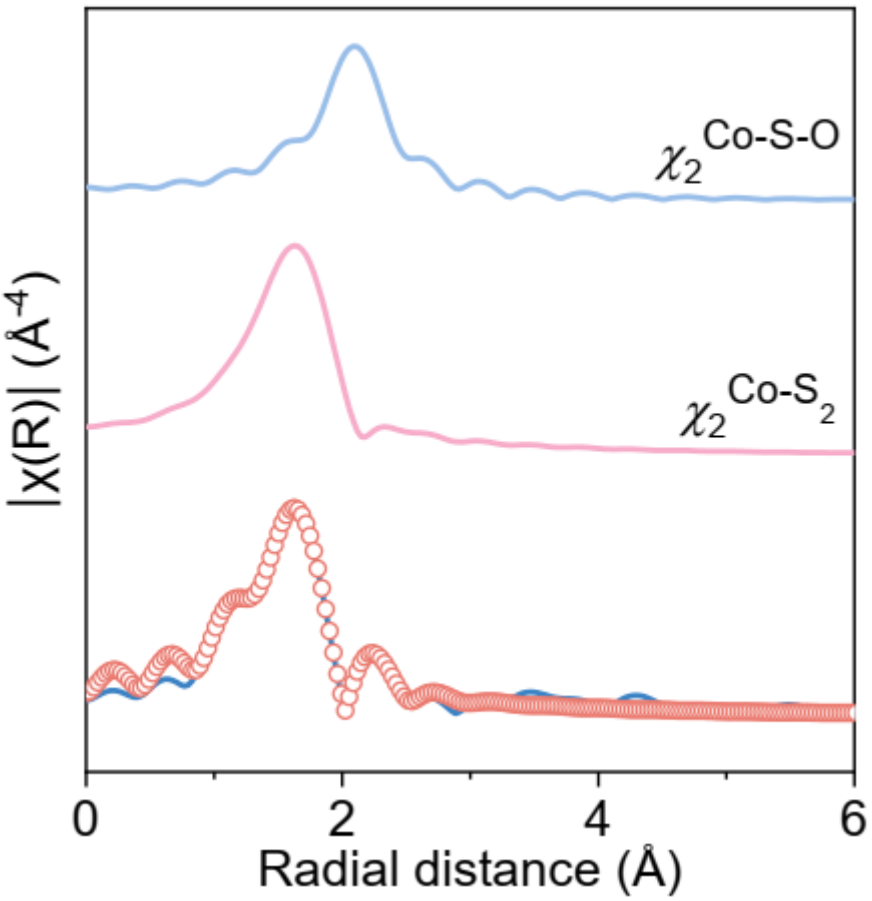

Supplementary Figure 23. Detailed EXAFS fitting of Co_s-SO-Ru at Co K-edge, inset curves are the Co-S and Co-S-O path signals (χ_2) involved in the total fitting curve. All the original EXAFS data are processed without phase corrections.

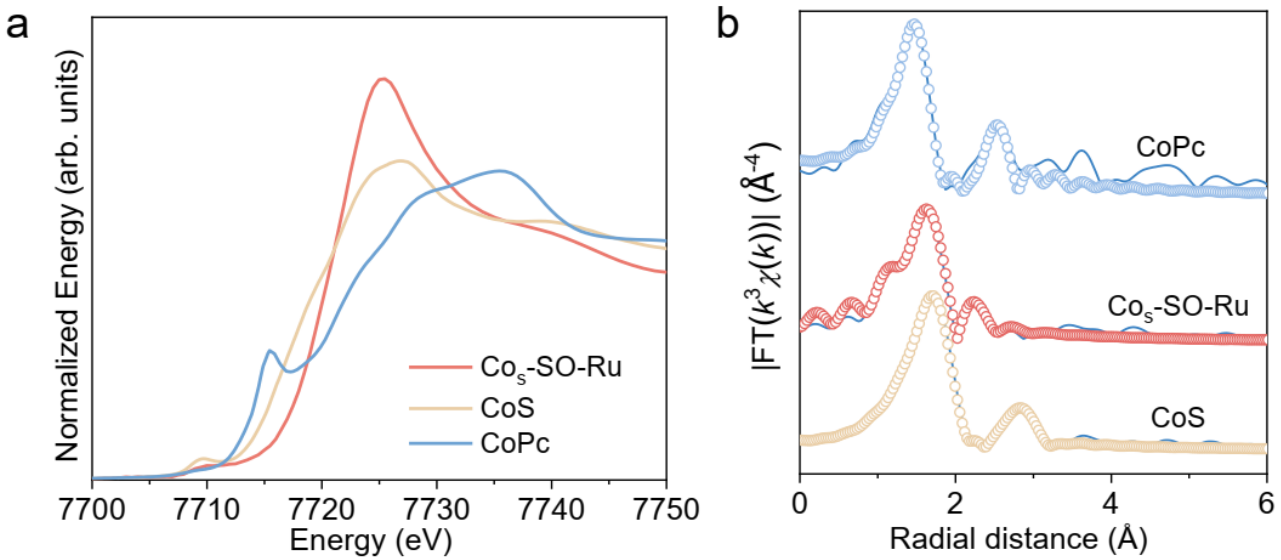

Supplementary Figure 24. a XANES spectra taken at Co *K*-edge for CoPc, CoS, and Co_s-SO-Ru. **b** FT-EXAFS in R-space and corresponding fitting curves. All the original EXAFS data are processed without phase corrections.

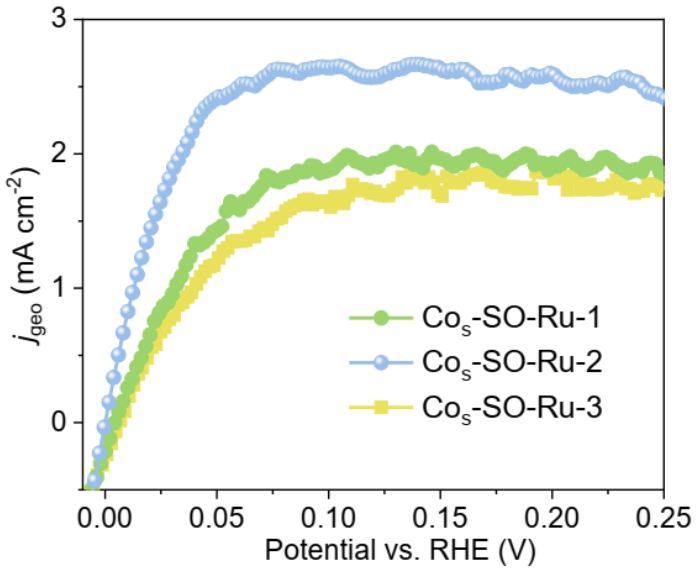

Supplementary Figure 25. HOR polarization curves of different catalysts in H_2-saturated 0.1 M KOH.

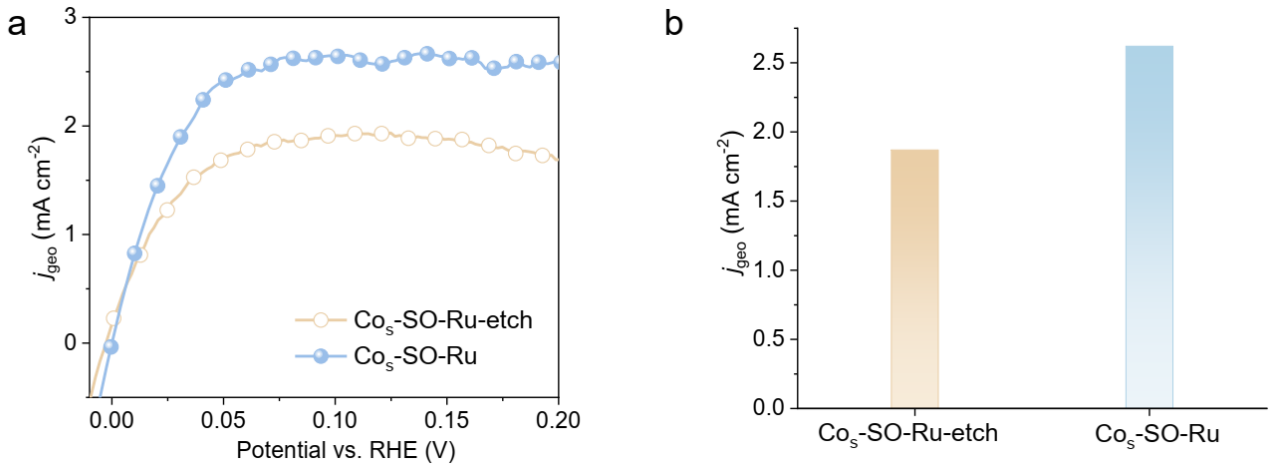

Supplementary Figure 26. a HOR polarization curves of different catalysts in H_2-saturated 0.1 M KOH. **b** The current density of different catalysts obtained at an overpotential of 50 mV.

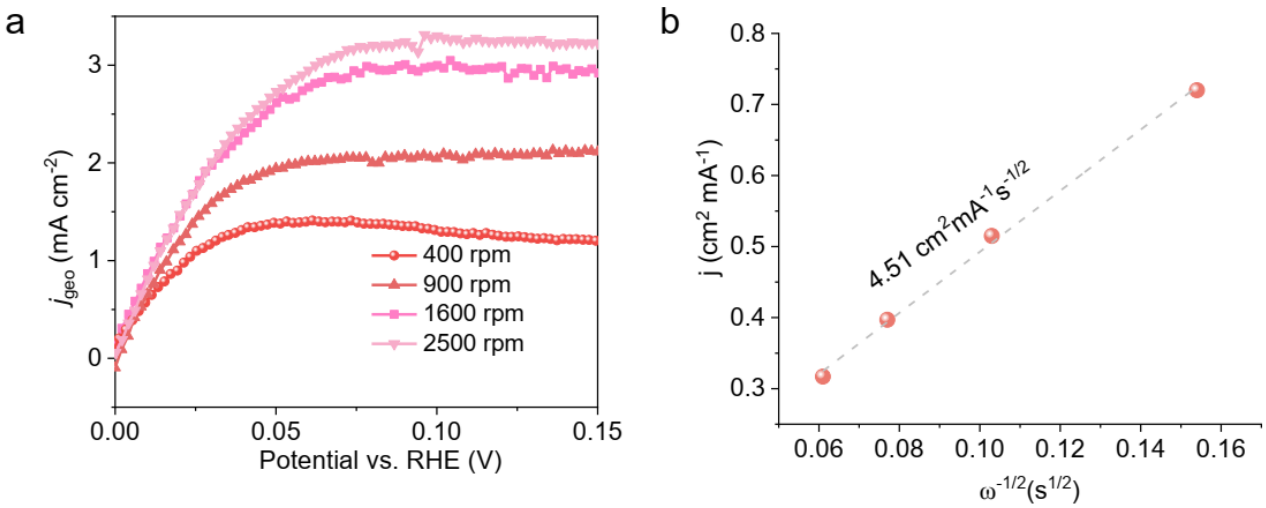

Supplementary Figure 27. **a** HOR polarization curves of Co_s-SO-Ru at different rotating speeds. **b** The slope for HOR at Co_s-SO-Ru electrode.

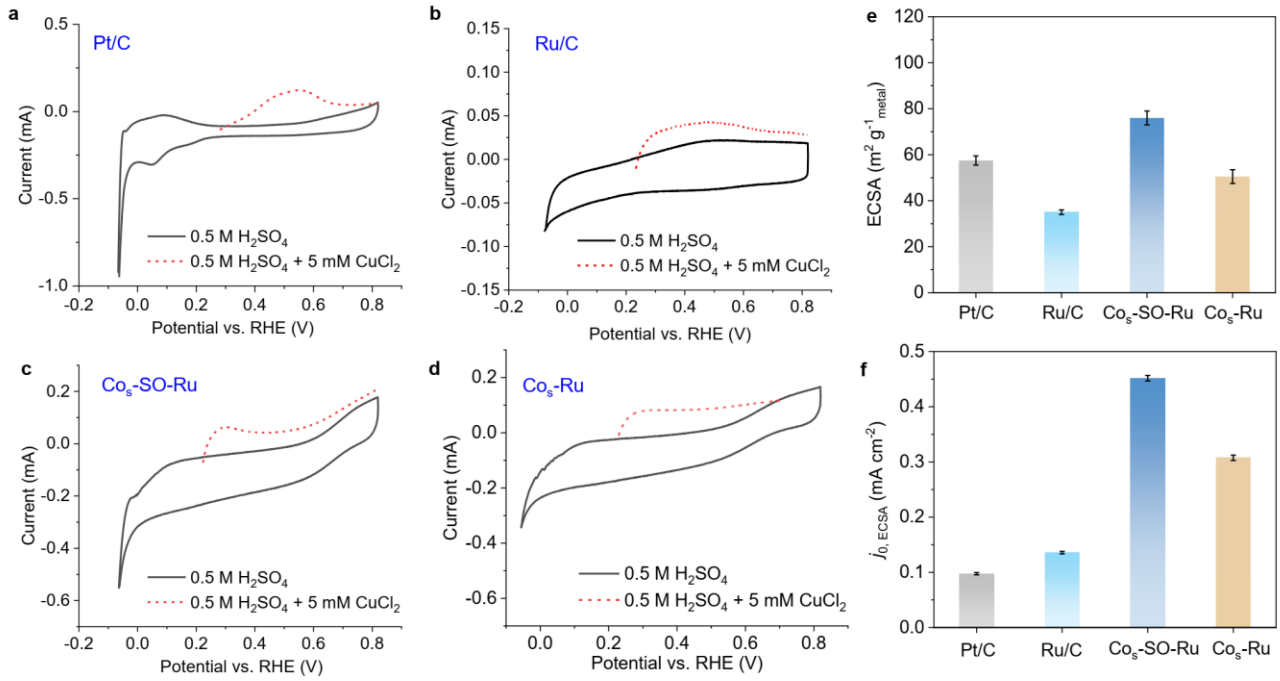

Supplementary Fig. 28 Calculation of ECSA via the Cu underpotential deposition (Cu-UPD) methods for **a** Pt/C, **b** Ru/C, **c** Co_s-SO-Ru, and **d** Co_s-Ru. **e** The summary of the ECSA value for different catalysts. **f** The calculated $j_{0,\,ECSA}$ of different catalysts. The CV curves are performed in 0.5 M H_2SO_4 electrolyte in the absence (black) and presence (red) of 5 mM $CuCl_2$. As exhibited, the Co_s-SO-Ru exhibits higher ECSA (76 $m^2\ g^{-1}$) than that of Co_s-Ru (50 $m^2\ g^{-1}$), which may be attributed to that the S=O bonds would depress the agglomeration of Ru clusters during pyrolysis process. Moreover, the Co_s-SO-Ru shows the highest ECSA normalized exchange current density ($j_{0,\,ECSA}$, 0.451 mA cm^{-2}) than that of Co_s-Ru (0.307 mA cm^{-2}), Pt/C (0.097 mA cm^{-2}), and Ru/C (0.135 mA cm^{-2}), indicating outstanding HOR catalytic activity of Co_s-SO-Ru.

To obtain monolayered Cu atoms on metallic sites, the Pt/C and Ru-based electrodes were polarized at underpotentially deposited potentials for 100 s in 0.5 M H_2SO_4 with 5 mM $CuCl_2$. The Cu-UPD stripping processes were conducted via oxidation of the monolayered Cu between 0.2-0.7 V. The ECSA was calculated via the integral areas of Cu-UPD peaks (Q_{Cu}) with the subtraction of the background and a charge density of 420 μC cm^{-2} (Q_s):

$$ECSA\left(m^2_{metal}/g\right) = Q_{Cu}/(M_{metal} * Q_s)$$

where the M_{metal} is the loaded metal mass on the working electrode.

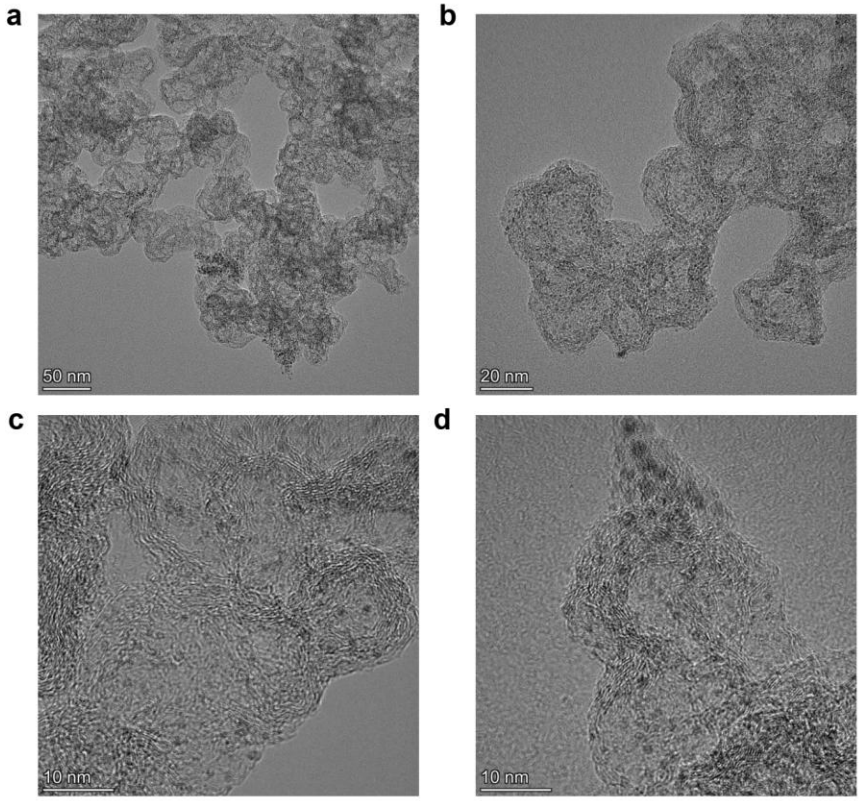

Supplementary Figure 29. a-d TEM images of the nanocarbon-supported Co_s-SO-Ru-after.

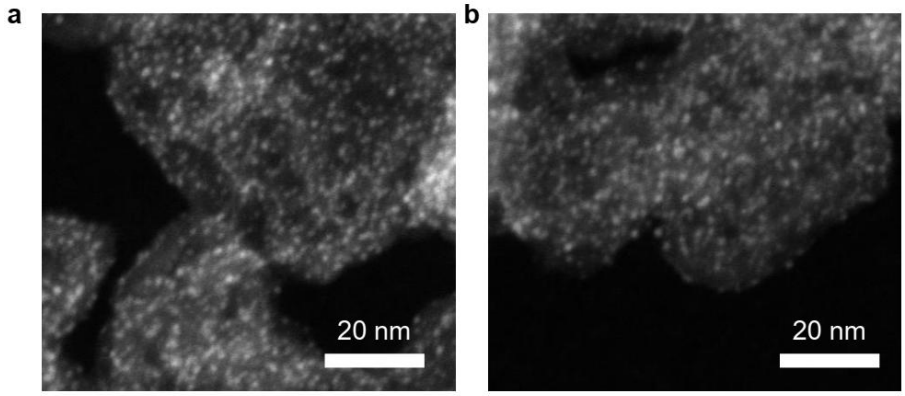

Supplementary Figure 30. a, **b** HAADF-STEM images of the nanocarbon-supported Co_s-SO-Ru-after.

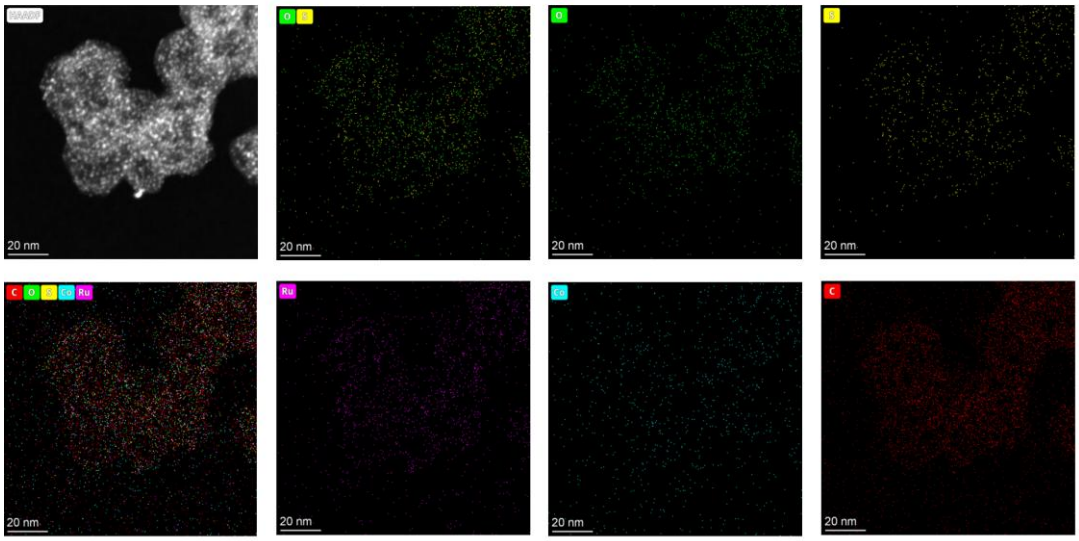

Supplementary Figure 31. HAADF-STEM image of Co_s-SO-Ru-after and corresponding EDX mappings.

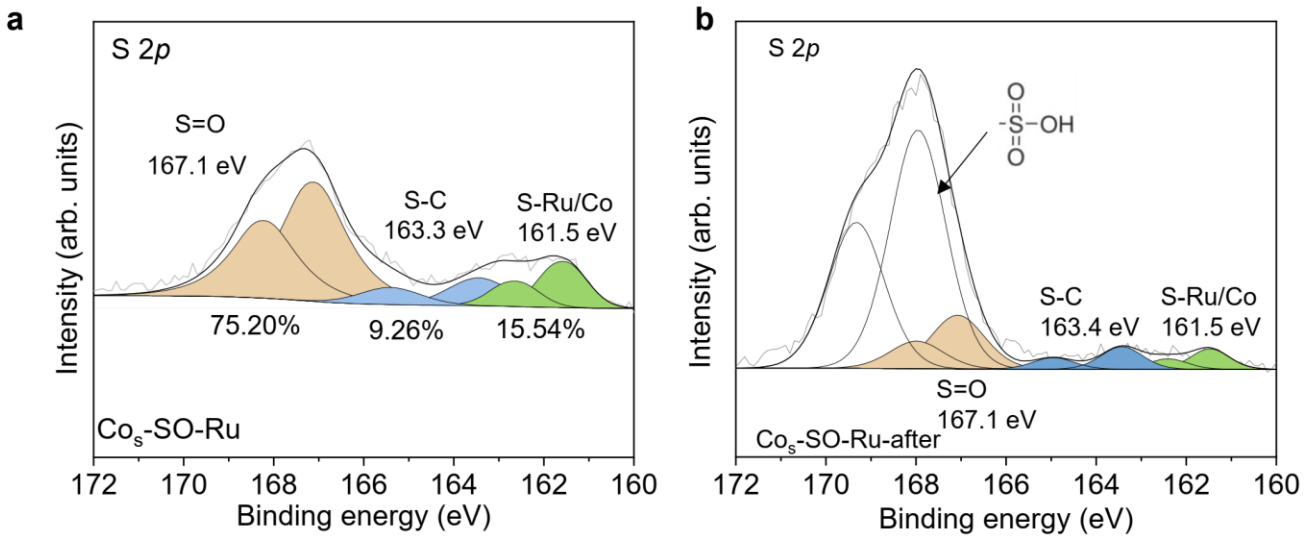

Supplementary Figure 32. XPS spectra of **a** Co_s-SO-Ru and **b** Co_s-SO-Ru-after in S 2*p* regions.

It should be noted that the strong peak at 168.1 eV in **b** would be attributed to presence of -SO_3H groups due to the Nafion polymers covering the surface of catalysts.

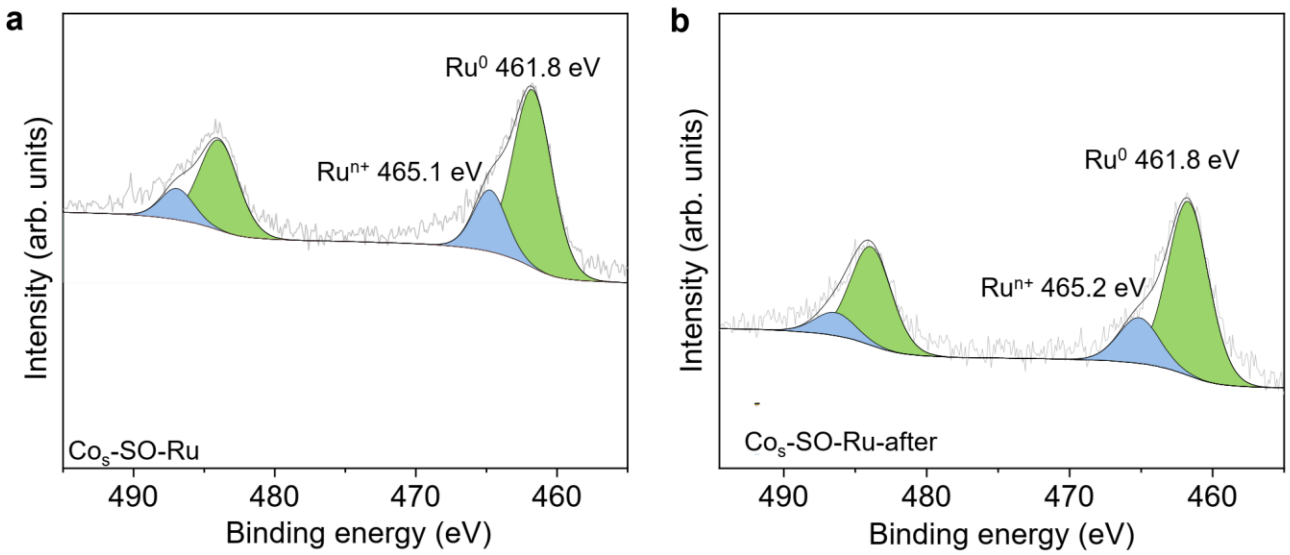

Supplementary Figure 33. XPS spectra of **a** Co_s-SO-Ru and **b** Co_s-SO-Ru-after in Ru 3*p* regions.

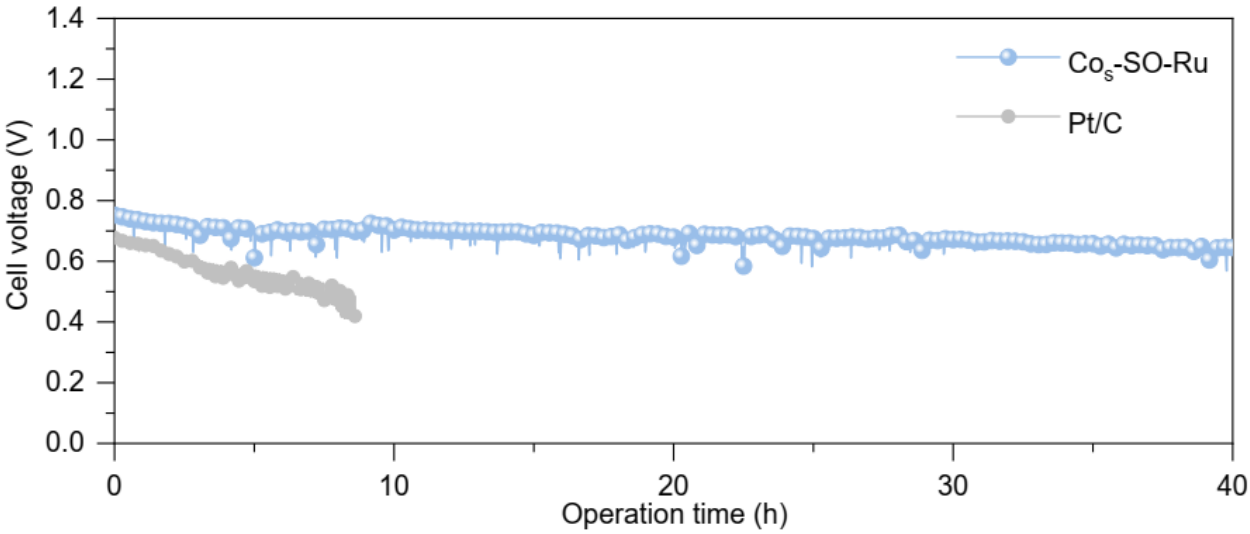

Supplementary Figure 34. The long-term durability test for HEMFCs using Co_s-SO-Ru or Pt/C as anode with current density of 500 mA cm^{-2}.

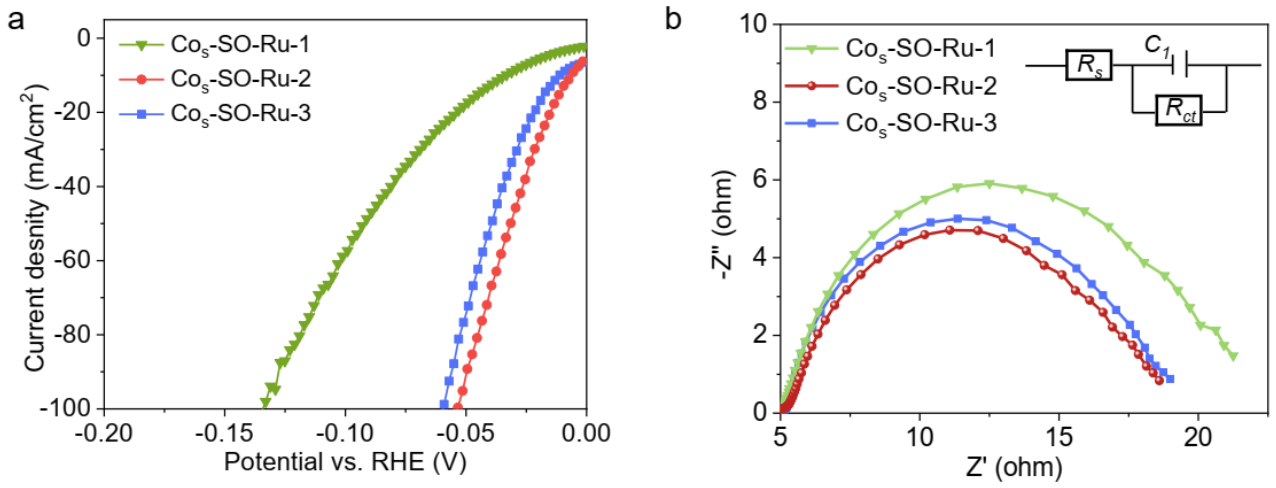

Supplementary Figure 35. a Comparison of HER polarization curves of Co_s-SO-Ru-1/2/3 in 1.0 M KOH. **b** The electrochemical impedance spectra of different samples in 1.0 M KOH.

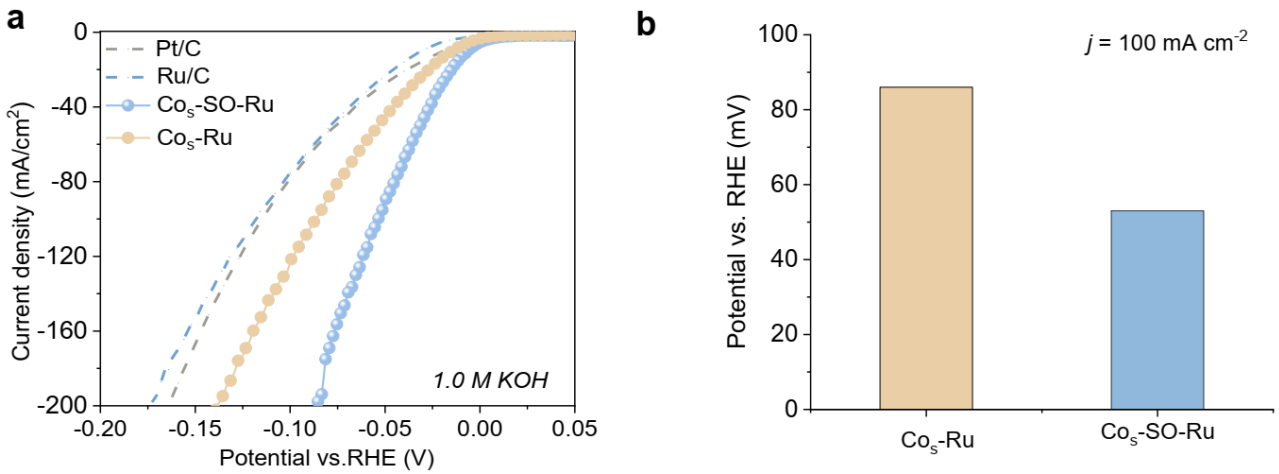

Supplementary Figure 36. a Comparison of HER polarization curves of different catalysts in 1.0 M KOH. **b** The overpotentials of different catalysts with current density of 100 mA cm^{-2}.

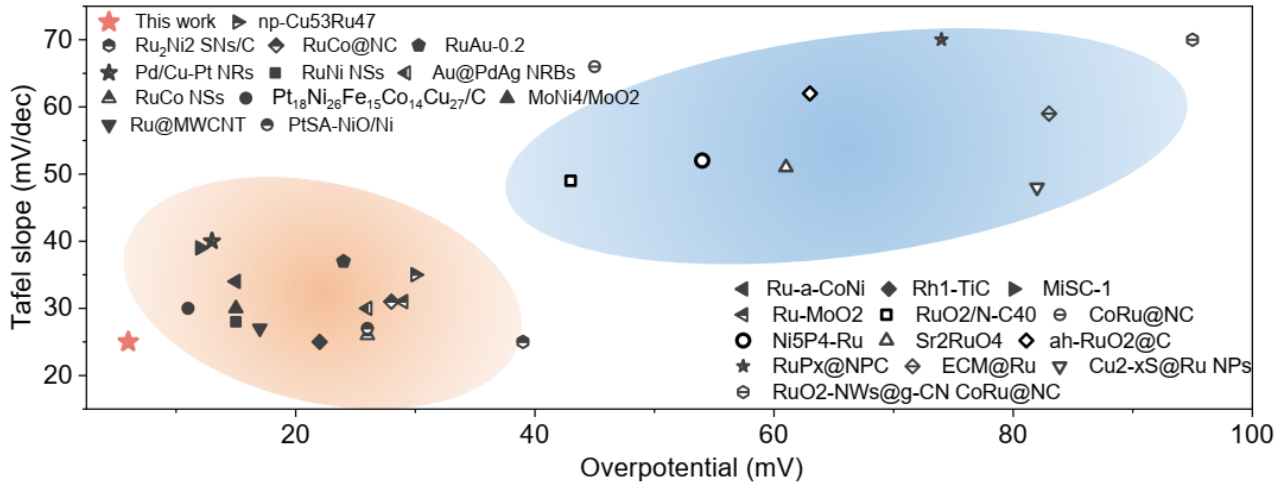

Supplementary Figure 37. The comparison of the Tafel slope and overpotential of Co_s-SO-Ru and other Ru-based materials.

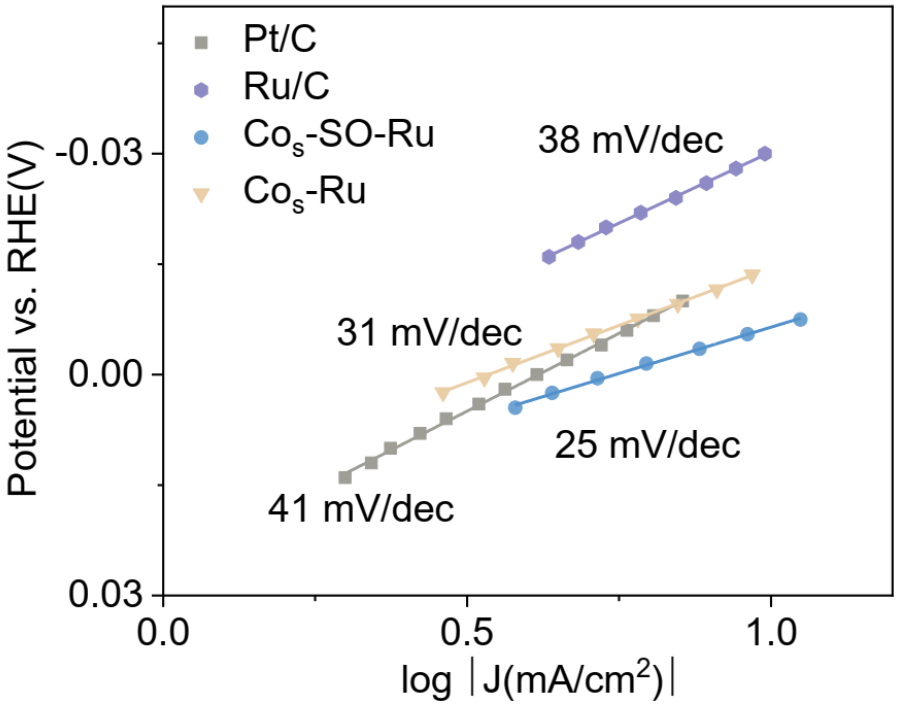

Supplementary Figure 38. The Tafel slope of different samples.

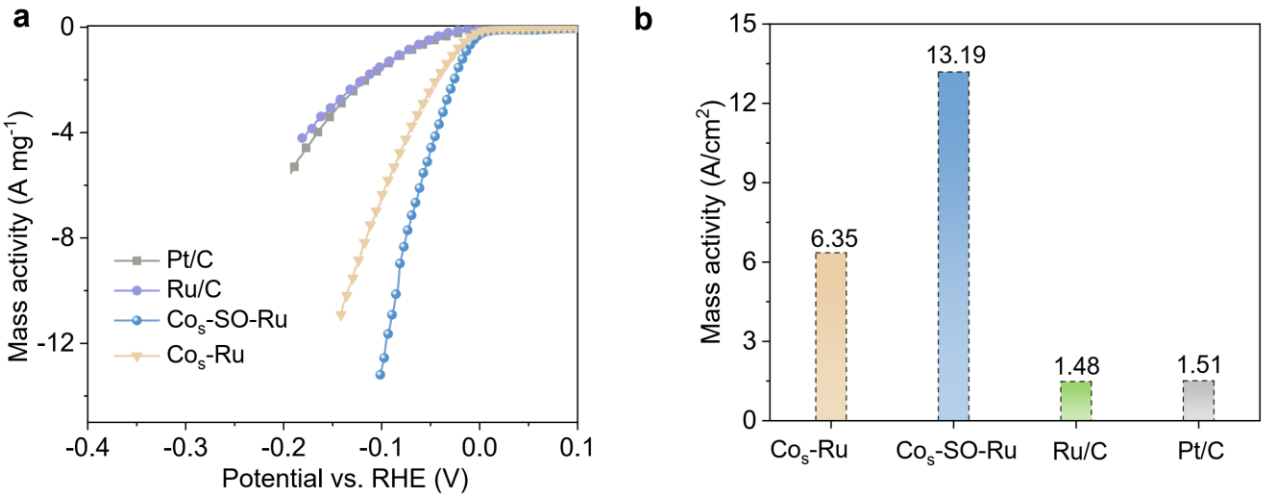

Supplementary Figure 39. a The mass activity of different catalysts in alkaline conditions that normalized by the noble metal mass. **b** The mass activity of different catalysts obtained with potential of -0.1 V.

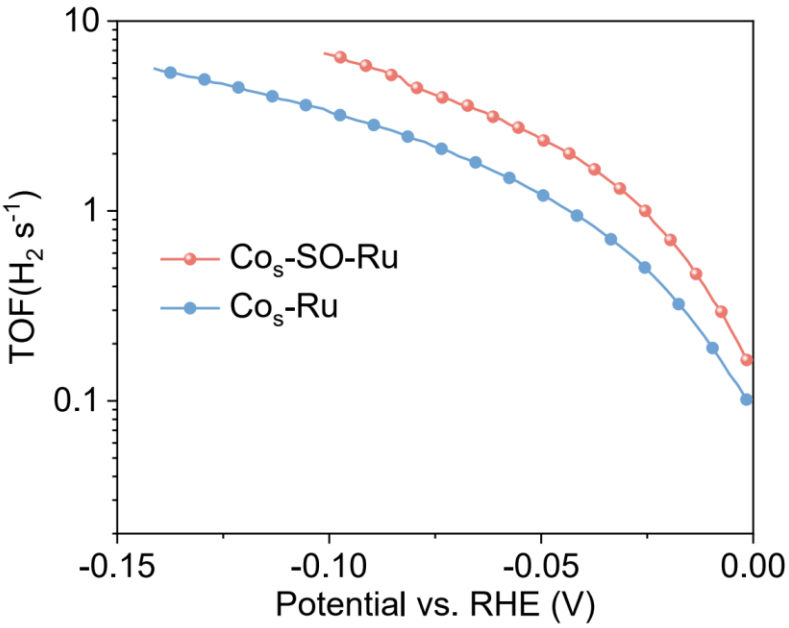

Supplementary Figure 40. The turnover frequency (TOF) of different catalysts in alkaline conditions is normalized by the noble metal mass.

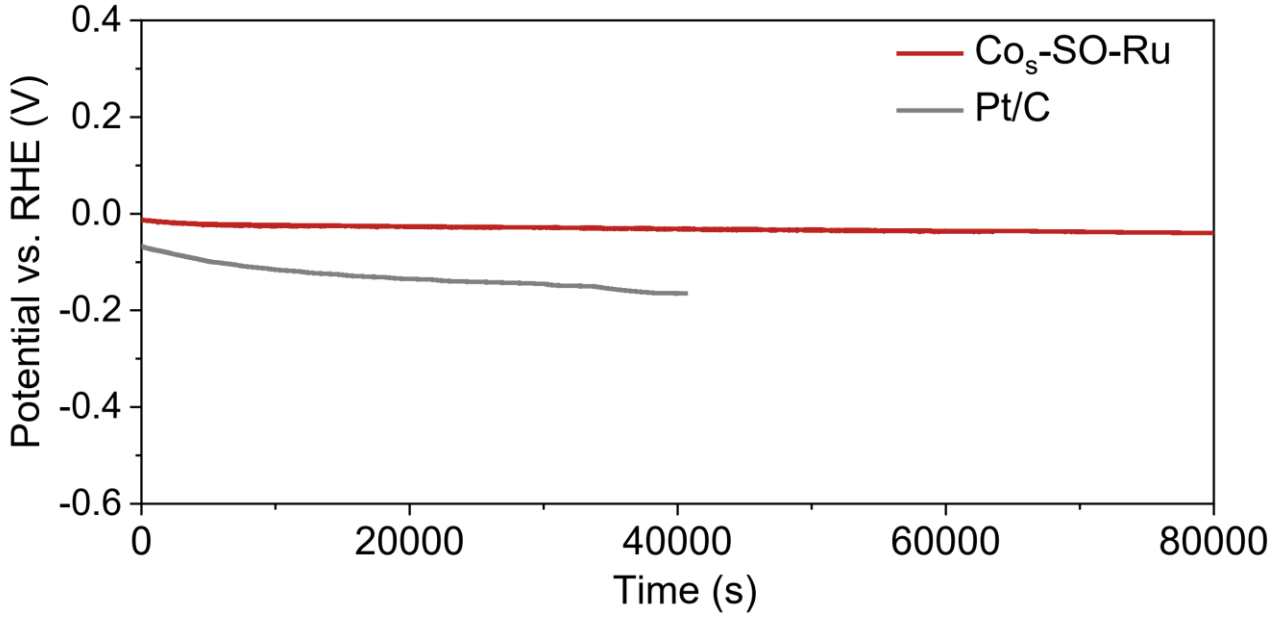

Supplementary Figure 41. Chronopotentiometric curves of Co_s-SO-Ru and Pt/C in alkaline condition.

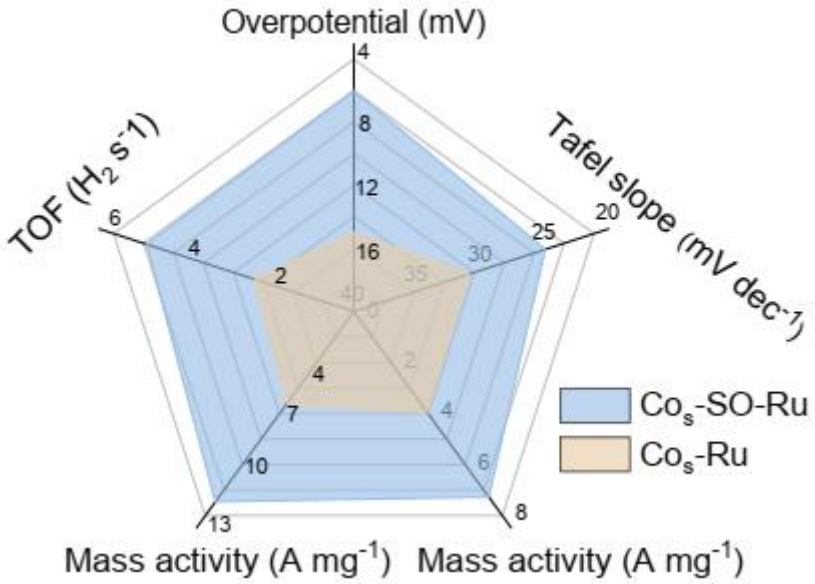

Supplementary Figure 42. Comparison of overpotential, TOFs, Mass activity, and Tafel slope for different catalysts.

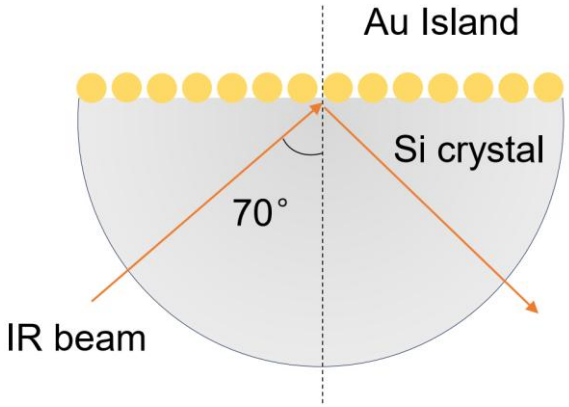

Supplementary Figure 43. Schematic illustration of in situ ATR-SEIRAS tests.

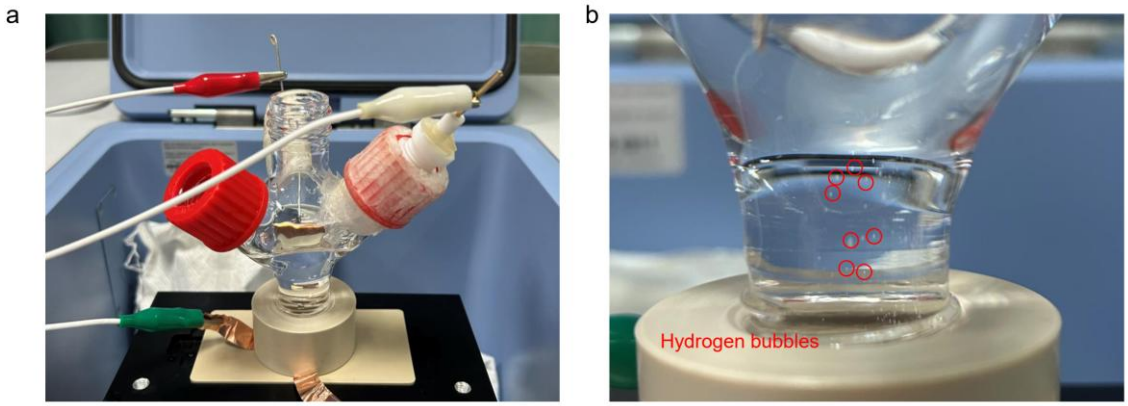

Supplementary Figure 44. a The photograph of in situ ATR-SEIRAS experimental setup. **b** The hydrogen bubbles generated during ATR-SEIRAS tests.

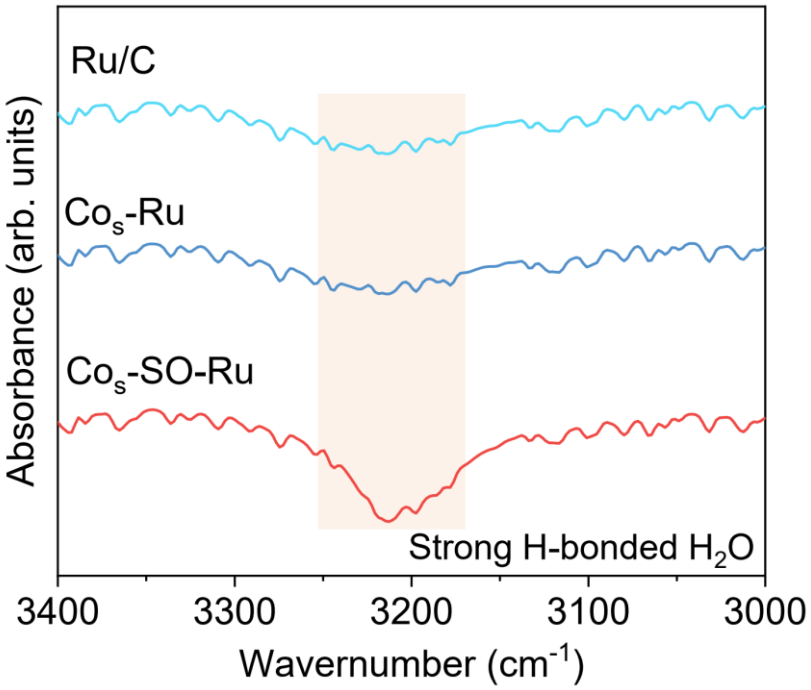

Supplementary Figure 45. The FT-IR spectra of different catalysts. As shown, the Co_s-SO-Ru catalyst exhibits strongly hydrogen-bond H_2O, which can be attributed to the adsorbed H_2O in air.

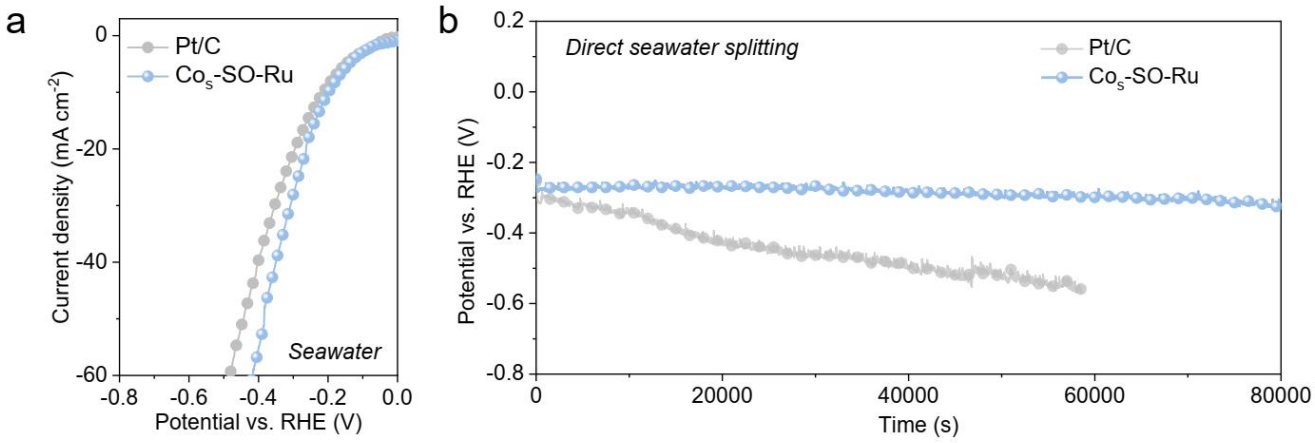

Supplementary Figure 46. a HER curves of different catalysts in seawater conditions. **b** Chronopotentiometric curves for direct seawater dissociation.

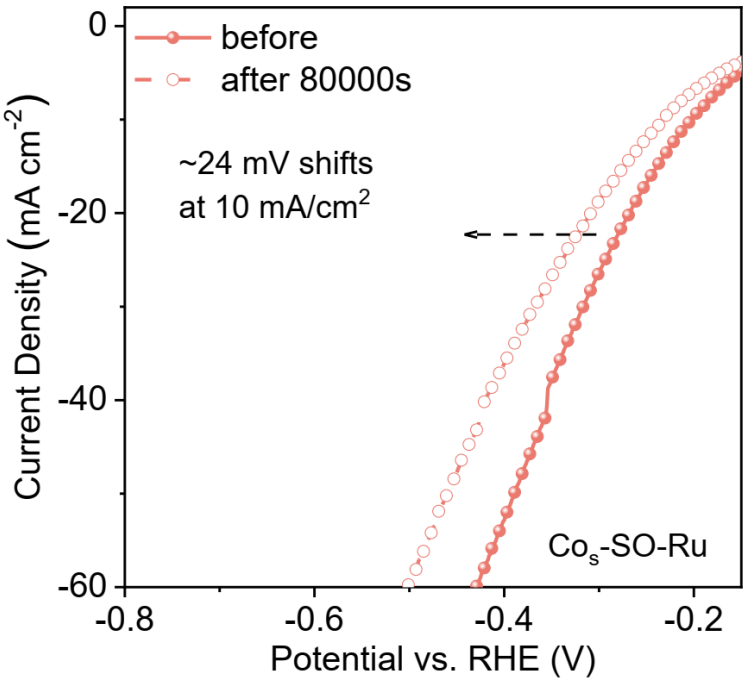

Supplementary Figure 47. The LSV curves of Co_s-SO-Ru before and after long-term tests in seawater condition.

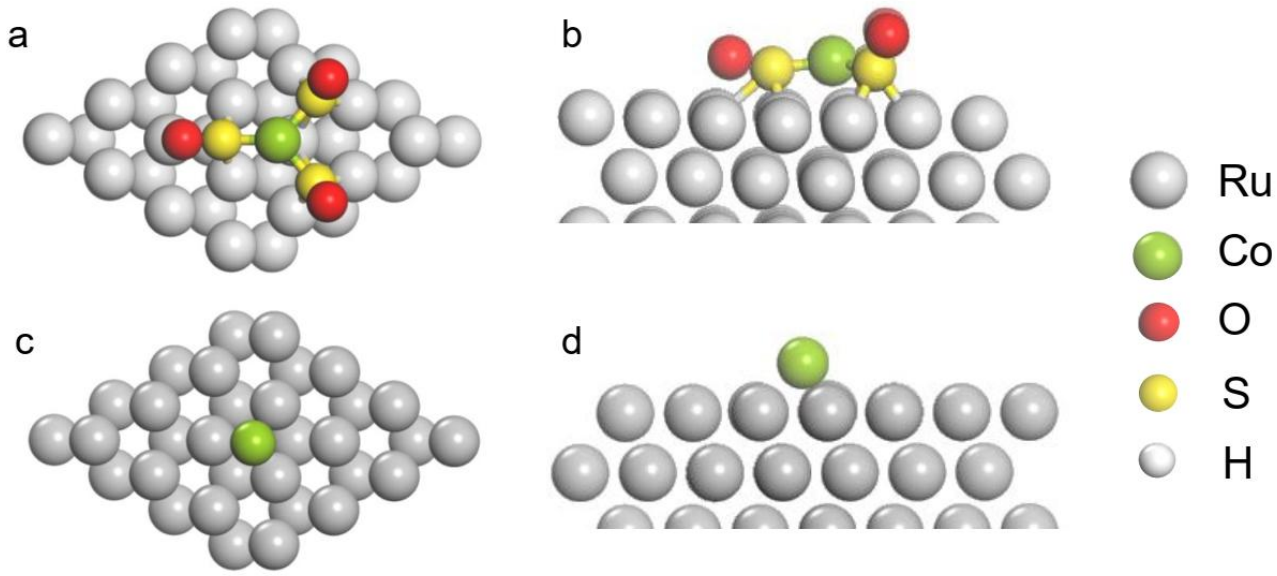

Supplementary Figure 48. The theoretical structures of **a**, **b** Co_s-SO-Ru and **c**, **d** Co_s-Ru.

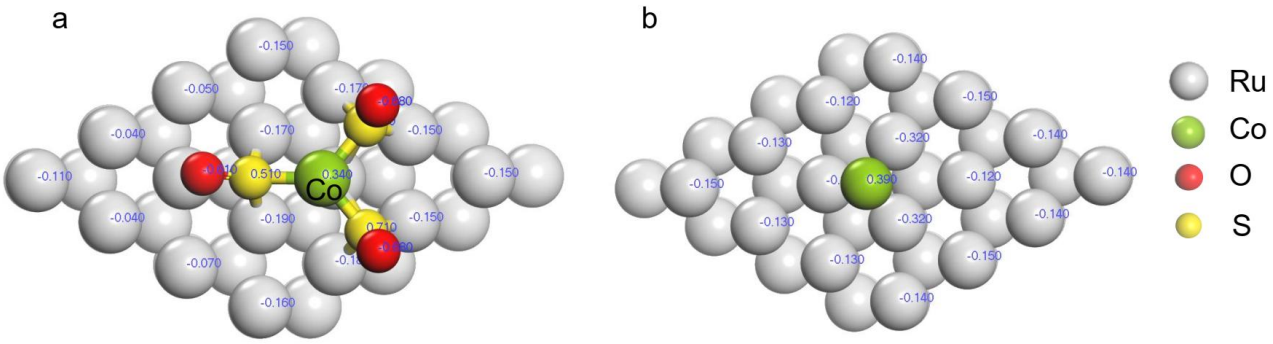

Supplementary Figure 49. The calculated charge distribution of **a** Co_s-SO-Ru and **b** Co_s-Ru.

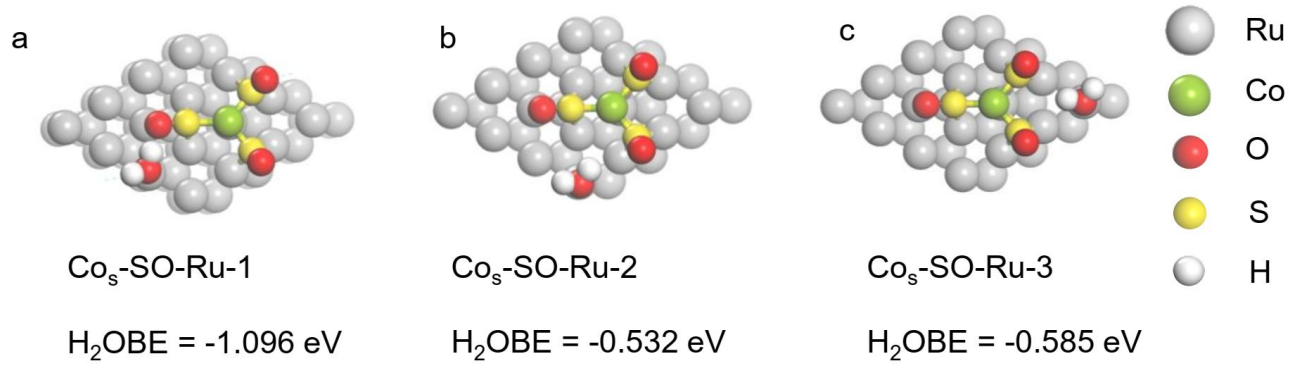

Supplementary Figure 50. a-c The H_2O* binding energy on different sites of Co_s-SO-Ru.

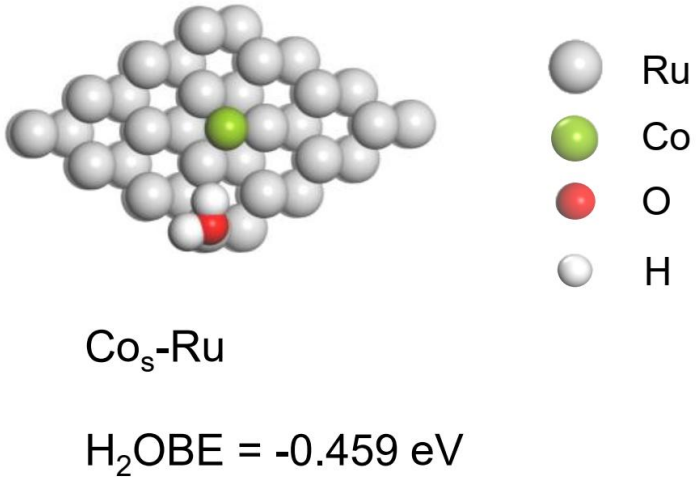

Supplementary Figure 51. The H_2O* binding energy on Co_s-Ru.

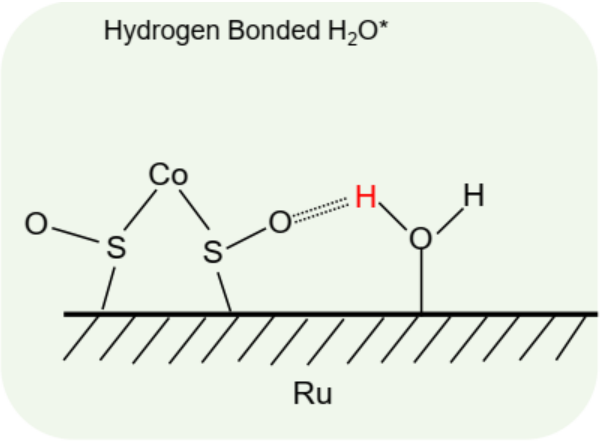

Supplementary Figure 52. The schematic illustration of the strongly H-bond water configuration.

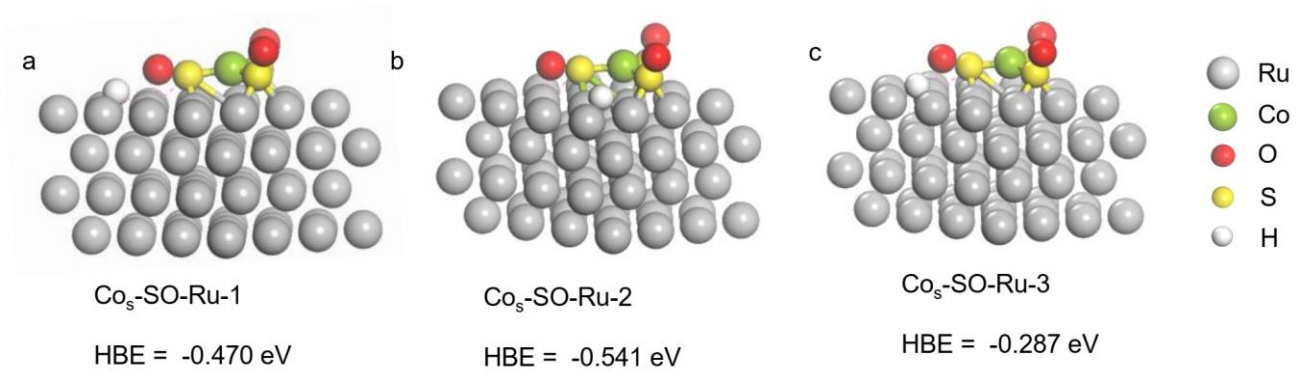

Supplementary Figure 53. a-c The H* binding energy on different Ru sites of Co_s-SO-Ru.

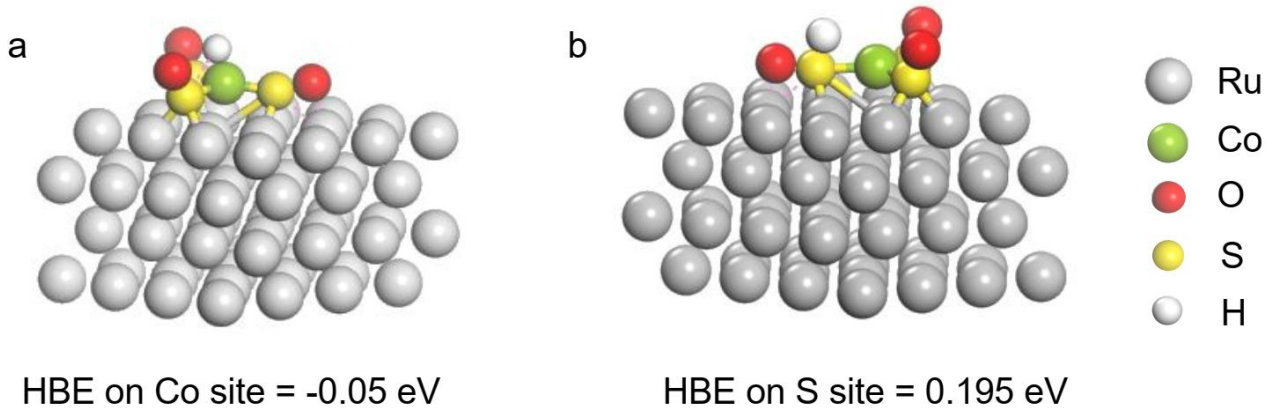

Supplementary Figure 54. The H* binding energy on **a** Co and **b** S sites of Co_s-SO-Ru.

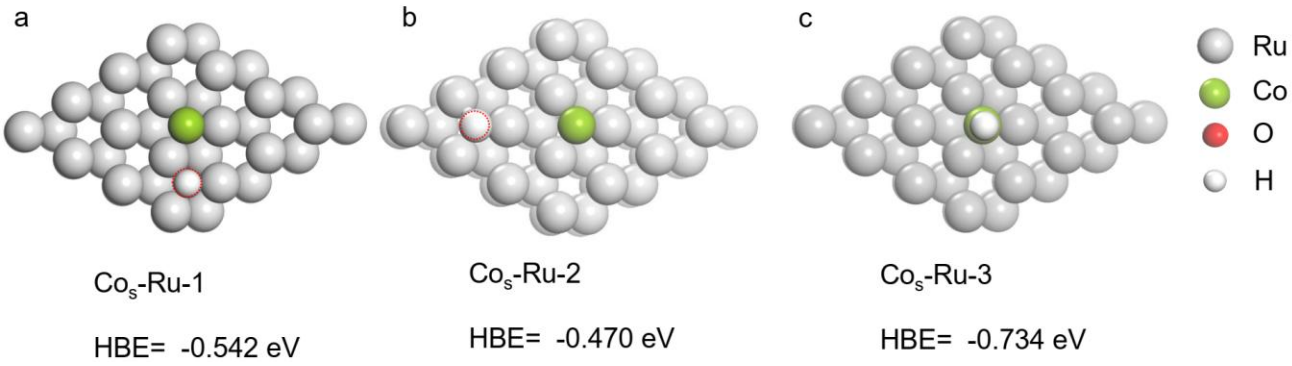

Supplementary Figure 55. a-c The H* binding energy on different Ru sites of Co_s-Ru.

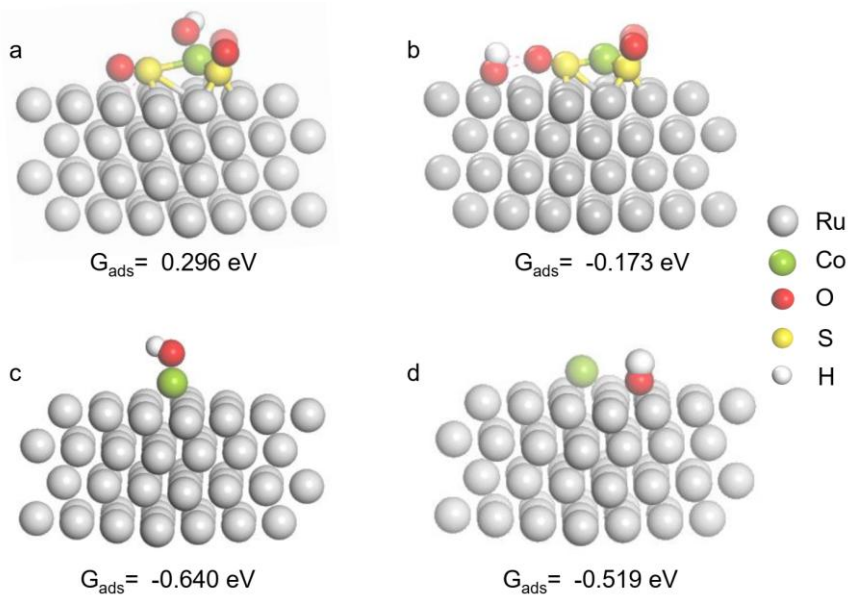

Supplementary Figure 56. a-d The Gibbs free energy of OH* on different Ru sites of Co_s-SO-Ru and Co_s-Ru.

Supplementary Tables

Supplementary Table 1. The contents of C, O, N, S, Co, and Ru species in the Co_s-SO-Ru catalyst were obtained from the XPS results.

Co_s-SO-Ru	**Contents (wt.%)**	**Contents (at.%)**
C	83.39	91.28
N	0.88	0.74
O	7.58	6.32
S	1.22	0.51
Co	1.10	0.25
Ru	5.83	0.85

Supplementary Table 2. The contents of C, O, N, Co, and Ru species in the Co_s-Ru catalyst were obtained from the XPS results.

Co_s-Ru	**Contents (wt.%)**	**Contents (at.%)**
C	84.15	92.79
N	1.26	1.09
O	5.89	4.89
Co	1.00	0.22
Ru	7.70	1.01

Supplementary Table 3. EXAFS fitting parameters at the Ru *K*-edge for various samples（S_0^2=0.75）

Samples	shell	CN	R(Å)	σ^2	ΔE_0	R factor
Ru foil	Ru-Ru	12	2.68±0.01	0.0041	-4.8±0.7	0.01
RuO_2	Ru-O	5.5±0.6	1.97±0.01	0.0021	4.3±1.7	0.008
	Ru-Ru	7.8±2.6	3.16±0.02	0.0087	4.4±2.5	
	Ru-Ru	4.4±1.3	3.60±0.01	0.0032	12.0±2.5	
Co_s-SO-Ru	Ru-S	2.0±1.2	1.99±0.04	0.0070	2.6±4.4	0.023
	Ru-Ru	2.4±0.7	2.68±0.04	0.0134		

[a]*N*: coordination numbers; [b]*R*: bond distance; [c]σ^2: Debye-Waller factors; [d] ΔE_0: the inner potential correction. *R* factor: goodness of fit. S_0^2 was set to 0.75, according to the experimental EXAFS fit of Ru foil reference by fixing CN as the known crystallographic value; δ: percentage.

Supplementary Table 4. EXAFS fitting parameters at the Co *K*-edge for various samples（S_0^2=0.75）

Samples	**shell**	**CN**	**R(Å)**	**σ^2**	**ΔE_0**	**R factor**
Co foil	Co-Co	12	2.49±0.02	0.0063	7.4±0.4	0.001
Co_3O_4	Co-O	5.2±0.5	1.91±0.01	0.0027	-8.1±1.6	0.003
	Co-Co	4.7±1.6	2.86±0.01	0.0038		
	Co-Co	9.1±2.2	3.36±0.01	0.0062		
CoS	Co-S	6.4±0.1	2.21±0.01	0.0089	-8.4±0.4	0.001
	Co-Co	6.0±0.4	3.25±0.01	0.0113		
Co_s-Ru	Co-O	3.0±0.5	1.92±0.02	0.0054	-5.0±2.7	0.020
	Co-Ru	1.0±0.3	2.51±0.09	0.0129		
Co_s-SO-Ru	Co-N	0.8±0.4	1.86±0.05	0.0027	-5.1±2.0	0.003
	Co-S	2.8±0.5	2.23±0.01	0.0141		
	Co-S-O	3.0	2.80±0.03	0.0049		

[a]*N*: coordination numbers; [b]*R*: bond distance; [c]σ^2: Debye-Waller factors; [d] ΔE_0: the inner potential correction. *R* factor: goodness of fit. S_0^2 was set to 0.75, according to the experimental EXAFS fit of Ru foil reference by fixing CN as the known crystallographic value; δ: percentage.

Supplementary Table 5. Comparison of mass-normalized HOR activities with various recently reported state-of-the-art noble-metal-based catalysts in 0.1 M KOH.

Catalysts	Catalysts loading (μg cm^{-2})	$j_{k,m}$ (A mg_{metal}^{-1})	Reference
Co_s-SO-Ru	14.5	3.44	***This work***
Co_s-Ru	17.5	1.38	***This work***
$Mn_1Ox(OH)y$@Ru/C	230	0.29	***Nat. Catal.*** 3, 454-462 (2020)
Ru-Cr_1(OH)x-1.1	60	0.43	***Nat. Commun.*** 13, 5894 (2022).
Ru/RuO_2-180	20	0.92	**Adv. Mater.** 2023, 35, 2208821.
Ru-Ru_2P/C	8.33	1.26	***Angew. Chem. Int. Ed.*** 2022, 63, 202215585
Ru/VOC	18.47	3.44	***J. Am. Chem. Soc.*** 2023, 145, 27867-27876
Ru-V_2O_3/OC	22.5	1.02	
$RuNi_1$	8.8	2.7	**Nano Lett.** 2020, 20, 3442-3448
Ru_2P/C	6.45	0.877	***Angew. Chem. Int. Ed***. 2024, 63, e202406888.
PtRu/Mo_2C–W_2C	13	0.40	**ACS Catal.** 11, 932-947 (2021)
RuP/NOC	18.1	3.25	**Adv. Mater. Interfaces** 2022, 9, 2102193.
O-Pt_3In/rGO[a]	10	2.306	***J. Am. Chem. Soc.*** 2024, 146, 29, 20323–20332
Pt NCs[a]	10	2.128	***Nat. Commun.*** 2022, 13, 1596.
PtMo NPs/C[a]	/	0.805	***Adv. Mater. 2023,*** 35, e2211854
$Co_{0.2}Ru_{0.7}Pt_{0.1}$/PNC[a]	15	1.84	***Angew. Chem., Int. Ed.*** 2023, 62, e202306881.
La_1Pt@HCS[a]	10	2.42	***Nat. Commun.*** 2023, 14, 3767
PmPt@IrPd[a]	9	1.05	***J. Am. Chem. Soc.*** 2023, 145, 4088-4097.
HEA-PdNiRuIrRh[a]	6.98	3.25	***Angew. Chem. Int. Ed.*** 2023, 62, e202217976
Pt SACs/CrN[a]	4.5	2.8	***Adv. Mater.*** 2023, 35, 2208799
Ni-Ir(BSC)/G[a]	31.8	0.33	***J. Am. Chem. Soc.*** 2023 145 (25), 13805-13815

[a] Pt or Ir-based catalysts for alkaline HOR.

Supplementary Table 6. Comparison of exchange current density and mass-normalized HOR activity with previously reported state-of-the-art noble-metal-based catalysts in 0.1 M KOH.

Catalysts	Scan rate ($mV\ s^{-1}$)	j_0 ($mA\ cm^{-2}$)	Mass-normlized $j_{0,m}$ ($mA\ mg^{-1}$)	Reference
Co_s-SO-Ru	5	3.51	280	***This work***
Co_s-Ru	5	2.45	140	***This work***
Pt_6NCs/C	5[a]	3.23	/	***Nat.Commun***. 13, 1596 (2022)
Ru colloidosomes	5[a]	2.86	50.18	***J. Am. Chem. Soc.*** 11138-11147 (2022)
Ru@TiO_2	10	2.0	79.78	***Nat. Catal.*** 3, 454-462 (2020)
Ni-H_2-NH_3	8.33	~1.10	21.95	***Nat. Mater.*** 21, 804-810 (2022)
Ru_2P	10	1.98	389	***Angew. Chem. Int. Ed***. 2024, 63, e202406888.
RuP	10	1.13	207	
PdCu/C-500 °C	1	1.63	127.62	***J. Am. Chem. Soc.*** 140, 16580-16588 (2018)
$Ir_3Pd_1Ru_6$/C	5	2.55	728.57	***J. Am. Chem. Soc.*** 139, 6807-6810 (2017).
RuP@RuP_2/C	10[a]	2.65	49.26	***Adv. Mater.*** 34, 2204624 (2022)
pc Pt with1-methylimidazole	10	~1.30	/	***Angew. Chem. Int. Ed.*** e202207197 (2022)

Supplementary Table 7. Comparison of ECSA-normalized HOR activity with previously reported state-of-the-art noble-metal-based catalysts in 0.1 M KOH.

Catalysts	ECSA-normlized $j_{0,ECSA}$ (mA cm_{metal}^{-2})	Reference
Co_s-SO-Ru	0.45	***This work***
Co_s-Ru	0.31	***This work***
$Mn_1O_x(OH)_y$@Ru/C	0.177	***J. Am. Chem. Soc.*** 2024 146 (24), 16619-16629
Pt/C	0.216	
Ru-CrO_x@CN	1.04	***Nat. Catal.*** 7, 441–451 (2024).
Ru@CN	0.95	
Ru-Cr_1(OH)x-2.2	0.28	***Nat. Commun.*** 2022, 13, 5894.
Ru_2P/C	0.389	***Angew. Chem. Int. Ed.*** 2024, 63, e202406888.
Rh_2Sb NBs	0.506	**Adv. Mater.** 2021, 33, e2105049.
Ir@Pd	0.294	***Adv. Mater.*** 2021, 33, 2105400.
di-RuNi MLNS/C	0.367	**Adv. Funct. Mater.** 2023, 33, 2210328.
HEA/C	1.19	***Angew. Chem. Int. Ed***. 2023, 62, e202217976.
PtRuNiCoFeMo HEA SNWs	0.969	**Nat. Commun.** 2021, 12, 6261.

Supplementary Table 8. Comparison of long-term HOR stability of Co_s-SO-Ru with various recently reported state-of-the-art noble-metal-based catalysts in 0.1 M KOH.

Catalysts	Reaction time (h)	Decreased activity (%)	Reference
Co_s-SO-Ru	200	8.8	***This work***
Ir_{SA}-Mo_2C/C	120	~5	***Nat. Commun.*** 15, 4236 (2024).
Ru@TiO_2	100	10.6	***Nat. Catal.*** 3, 454–462 (2020).
Ru-WC_x	40	6.63	***Angew. Chem. Int. Ed.*** 2023, 62, e202311937.
Ni/V_2O_3	16	1.5%	***Angew. Chem. Int. Ed***. 2023, 62, e202217275
$Mn_1O_x(OH)_y$@Ru/C	3	11.30	***J. Am. Chem. Soc.*** 2024, 146, 16619-16629
2H-Pd@2H-NiRh NRs	10	16	***J. Am. Chem. Soc***. 2024, 146, 24141-24149
Ru–$Cr_1(OH)_x$	50	12	***Nat. Commun.*** 13, 5894 (2022).
Ru/VOC	3	9.3	***J. Am. Chem. Soc.*** 2023, 145, 27867-27876
HEA	1	19	***Angew. Chem. Int. Ed***. 2023, e202217976
$Co_{0.2}Ru_{0.7}Pt_{0.1}$/PNC	1	14.20	***Angew. Chem. Int. Ed.*** 2023, e202306881
i-ZnIn-PR	2.778	6.1	***Nat. Commun.*** 15, 1097 (2024)
Ru-MnO/C	1	8.6	***Adv. Energy Mater.*** 2024, 2404266.
$(RuCo)_{NC+SAs}$/N-CNT	10	14.7	***Angew. Chem. Int. Ed.*** 2024, 63, e202404761.
$fcc_{0.42}$ Ru-Sn	14	35	***Energy Environ. Sci.***, 2024, 17, 5922-5930
Ru/RuO_2-180	8	10	***Adv. Mater***. 2023, 35, 2208821.

Supplementary Table 9. Comparison of the overpotential and Tafel slope between Co_s-SO-Ru and other state-of-the-art Ru-based HER catalysts.

Catalysts	Overpotential (mV)	Tafel slope (mV dec^{-1})	References
Co_s-SO-Ru	6	25	***This work***
np-$Cu_{53}Ru_{47}$	30	35	*ACS Energy Lett.* **5**, 192-199 (2020)
Ru_2Ni_2 SNs/C	39	25	*Nano Energy* **47**, 1-7 (2018).
RuCo@NC	28	31	*Nat. Commun.* **8**, 14969 (2017).
RuAu-0.2	24	37	*Adv. Energy Mater.* **9**, 1803913 (2019).
Pd/Cu-Pt NRs	13	40	*Angew. Chem. Int. Ed*. **56**, 16047-16051 (2017).
RuNi NSs	15	28	*Nano Energy* **66**, 104173 (2019).
Au@PdAg NRBs	26	30	*J. Am. Chem. Soc.* **138**, 1414-1419 (2016).
RuCo NSs	26	26	*Adv. Energy Mater.* **10**, 2002860 (2020).
$Pt_{18}Ni_{26}Fe_{15}Co_{14}Cu_{27}$/C	11	30	*Nat. Commun.* **11**, 5437 (2020).
$MoNi_4/MoO_2$	15	30	*Adv. Mater.* **29**, 1703311 (2017).
Ru@MWCNT	17	27	*Nat. Commun.* **11**, 1278 (2020).
PtSA-NiO/Ni	26	27	*Nat. Commun.* **12**, 3783 (2021).
Ru-a-CoNi	15	34	*Angew. Chem. Int. Ed*. **61**, e202114160 (2022).
Rh_1-TiC	22	25	*Angew. Chem. Int. Ed*. **60**, 19085-19091 (2021).
MiSC-1	12	39	*Adv. Energy Mater.* **11**, 2100141 (2021).
Ru-MoO_2	29	31	*J. Mater. Chem. A* **5**, 5475-5485 (2017).
RuO_2/N-C40	43	49	*Chem. Commun.* **54**, 4613-4616 (2018).
CoRu@NC	45	66	*Nanotechnology* **29**, 225403 (2018).
Ru_2P@PNC/CC-900	50	66	*ACS Appl. Energy Mater.* **1**, 3143-3150 (2018).
Ni_5P_4-Ru	54	52	*Adv. Mater.* **32**, 1906972 (2020).
Sr_2RuO_4	61	51	*Nat. Commun.* **10**, 149 (2019).
ah-RuO_2@C	63	62	*Nano Energy* **55**, 49-58 (2019).
RuP_x@NPC	74	70	*ChemSusChem* **11**, 743-752 (2018).

ECM@Ru	83	59	*Adv. Energy Mater.* **10**, 2000882 (2020).
Cu_2-xS@Ru NPs	82	48	*Small* **13**, 1700052 (2017).
RuO_2-NWs@g-CN CoRu@NC	95	70	*ACS Appl. Mater. Interfaces* **8**, 28678-28688 (2016).